University of Alberta

Simulations of Agitated Dilute Non-Newtonian Suspensions

Elorm Sekyi

A thesis submitted to the Faculty of Graduate Studies and Research in partial fulfilment of the requirements for the degree of
Master of Science
in
Chemical Engineering

Chemical and Materials Engineering Department

Fall 2009

Edmonton, Alberta

Examining Committee

Dr. Jos Derksen, Chemical & Materials Eng. Dept.

Dr. Suzanne Kresta, Chemical & Materials Eng. Dept.

Dr. Morris Flynn, Mechanical Eng. Dept.

Dedicated to

Christian, Nelly and Teddy

Abstract

Particle distribution and settling in suspensions with non-Newtonian liquids agitated with a Rushton turbine in a lab-scale tank have been studied. The rheology of the non-Newtonian liquids can be described by the power-law, Bingham and Herschel-Bulkley fluid models. The dynamics of the dispersed phase – settling particles (size 0.65mm) is modeled by a Lagrangian tracking approach while the liquid phase is resolved by the lattice-Boltzmann method.

Qualitative insight emerging from exploration of shear-thinning/thickening, Newtonian, yield-stress fluid models at Reynolds number, Re=$6 \times 10^3, 8.5 \times 10^3$ and 1.25×10^4 indicate that bottom particle concentration is highest in power-law liquids than in Newtonian; while yield stress fluids had more uniform particle concentration and least bottom concentration. Also, turbulent kinetic energy and viscous dissipation are highest in the Newtonian liquid. Extra viscous diffusion due to fluctuating non-Newtonian viscosity in the turbulent kinetic energy equation attributes to these differences.

Acknowledgements

The "smart" society of tomorrow will need more than formally trained engineers. It will require talented engineers committed to the continual improvement of existing competences through research and innovation in an ever engaging manner in delivering highly efficient smart products. This is both my inspiration and reason for pursuing a research degree. It took more than my will to make this happen and I am morally indebted to Dr. Volker Weiss, who taught me Advanced Physical Chemistry and much later, routinely through our emails encouraged and graciously recommended me in my grad school applications.

I also want to express my deepest appreciation towards my supervisor Dr. J.J. Derksen for his immense expertise, reliability and critical evaluations of my work. I will be forever grateful for his unlimited availability and strong commitments he has shown in the past couple of years, as this has enabled frequent intellectual dialogue and expedited the progress of this work.

The financial support from the University of Alberta, Chemical and Materials Engineering Dept. as well as Petro-Canada Ltd. has been of tremendous use and therefore sincerely appreciated.

Last but not the least, I will want to specially thank my family; each and every member of the Sekyi family has been and will remain a part of my story. I love you all.

Contents

List of Figures

List of Tables

Nomenclature

$\|A\|$	distance from anisotry, $(-)$
a_{ij}	anisotropy tensor, $(-)$
C_D	drag coefficient, $(-)$
D	impeller diameter, (m)
d_p	particle diameter, (m)
f_0	force per unit volume in streamwise direction of flow, $(kg/m^2/s^2)$
F_D	drag force, (kgm/s^2)
F_g	gravity force, (kgm/s^2)
F_{AM}	added mass force, (kgm/s^2)
g	gravity, (m/s^2)
H	plane height, (m)
I, II, III	invariants of a_{ij}, $(-)$
K	fluid consistency, $(kg/m/s^n)$
k	turbulent kinetic energy, (m^2/s^2)
M	number of particles, (-)
N	impeller speed, (rev/s)

n flow index, $(-)$

N_{js} just suspended speed, (rev/s)

R radius of impeller, (m)

r radial length, (m)

s constant in N_{js} equation, $(-)$

S_{ij} i,j-th component of the rate-of-strain tensor, (s^{-1})

s_{ij} i-jth component of the shear-rate determined from the turbulent fluctuating velocities, (s^{-1})

T tank size, (m)

t time, (s)

T_q torque, (Kgm^2/s^2)

y vertical height, (m)

y_1 width of the yielded region, (m)

$\mathbf{F}$ force vector, (kgm/s^2)

$\mathbf{x}_p$ particle position vector, (m)

$N_P = \frac{T\Omega}{\rho N^3 D^5}$ power number, $(-)$

$Re = \frac{\rho_l N D^2}{\eta_a}$ Reynolds number based on impeller, $(-)$

$Re = \frac{\rho_l u_{max} H}{\eta}$ Reynolds number, $(-)$

$Y = \frac{\tau_0}{\rho_l N^2 D^2}$ Yield stress number, $(-)$

u streamwise velocity, (m/s)

u_{max} max. velocity from exact solution, (m/s)

v	velocity in y-direction, (m/s)
v_p	particle velocity, (m/s)
V_{tip}	impeller tip velocity, (m/s)
u	absolute velocity, (m/s)
U	mean axial velocity, (m/s)
V	mean radial velocity, (m/s)
W	mean tangential velocity, (m/s)
Γ_i	collision operator in LBM, $(-)$
ν	constant kinematic viscosity in the LBM, $(-)$
c_i	velocity direction vector in i-th direction, $(-)$
m_i	multiciplicity for direction c_i, $(-)$
N_i	mass density in ith-direction, $(-)$
x	position vector, (m)
ν_a'	fluctuating kinematic viscosity, (m^2/s)
α	measure of shear-thinning index in eqn (3.6)
$\Delta\rho$	density difference between solid and liquid, (kg/m^3)
Δ	Spatial resolution, (m)
δ_{ij}	kronecker delta function in i, j directions, $(-)$
$\dot{\gamma}_a$	apparent shear-rate,(s^{-1})
$\dot{\gamma}_c$	critical shear-rate, (s^{-1})
ϵ	energy dissipation, (m^2/s^{-3})

η_a apparent dynamic viscosity, $(kg/m/s)$

η_K Kolmogorov length scale, (m)

η_r high end (zero shear) dynamic viscosity, $(kg/m/s)$

η_0, η_∞ zero- and infinite- shear dynamic viscosity in (3.4) and (3.5), $(kg/m/s)$

λ constant in Carreau model (3.4), (s)

$\lambda_1, \lambda_2, \lambda_3$ eigenvalues of a_{ij}, $(-)$

μ dynamic viscosity, $(kg/m/s)$

Ω angular revolution of impeller, (s^{-1})

Φ_m solids mass fraction, $(-)$

ρ_l liquid density, (Kg/m^3)

ρ_s particle density, (kg/m^3)

τ_0 yield stress, (Pa)

$\tau_{1/2}$ half value of shear-stress in eqn(3.6), (Pa)

τ_{ij} i, j-th component of stress tensor, (Pa)

$\tilde{\nu_a}$ instantaneous kinematic viscosity, (m^2/s)

1 Introduction

1.1 Computational Fluid Dynamics and Two-Phase Flows

Over the last few decades, computational fluid dynamics (CFD) has increasingly gained reputation as research and design tool. As a research tool, it can be used to uncover or corroborate insights about fluid flow that are challenging to measure experimentally or deduce from theory. When used as a design tool, CFD has the capability of reducing if not eliminating pilot scale testing and can serve as a guide towards equipment selection. The application of CFD in industrial processes can lead to improved product quality and minimal pollution.

CFD generally refers to the various numerical schemes, e.g. lattice-Boltzmann method, finite difference, finite element, spectral method etc, used in simulating fluid flow. In all schemes, the flow geometry along with its boundary conditions are specified; then this domain is discretized and the equations of motions are solved for in the domains.

Arguably, CFD is of tremendous advantage when it comes to two-phase stirred tank flow owing to the complex 3D turbulent structures generated by the impeller in stirred tank flow coupled with the presence of a second phase. Usually, in the modeling of such systems, two approaches exist [1]: Eulerian-Eulerian and Eulerian-Lagrangian. In the Eulerian-Lagrangian approach, the liquid phase is treated as a continuum and the dispersed phase is tracked as individual particles whose trajectories are solved by integrating the equations of motion. The Eulerian-

Eulerian approach regards both phases are interpenetrating and interacting continua. The equations of motion in this case are similar with each phase containing its volume fraction. This approach is known to be computational economical as it can handle large volume fractions of dispersed phase and convenient for implementing two-way coupling [2]. However, the Euler-Lagrangian method, by some comparison studies [3, 4] has proven to give more detailed particle flow field.

The Eulerian-Lagrangian modeling approach will be used in this thesis in the simulation of solid particles in turbulently agitated viscous non-Newtonian liquids. Direct numerical simulation[1] (DNS) of the liquid flow employed in this work is to a large extent beneficial [5, 6] since the impact of the non-Newtonian characteristics of the liquid on the flow will be examined at all scales of the flow.

The use and application of mechanical agitation employed in this work extends beyond the confines of academia; in fact it is a process widely used in several industries. Mostly, agitation takes place in a stirred vessel equipped with an impeller (also called agitator) used to generate large shear and contact area that facilitates the required homogenization, phase change, mass transfer, reaction, etc. When there is more than one component, then mixing is substituted for this term[2]. Together, agitation and mixing are central to the majority of process industries including, food, bio, paint, polymer, chemical, etc; and failures — emanating from poor design, lack of fundamental understanding — associated with these processes are in the range of billions of dollars per annum in the US alone [7].

In several applications the liquid phase is non-Newtonian. At other times, the liquid is Newtonian at start, then as the process goes on the liquid rheology becomes non-Newtonian either due to reactions as in fermentation or additives e.g. emulsions [8]. The impact of the non-Newtonian rheology in many instances is ignored.

[1] In DNS, all scales – time and length – are resolved directly without any turbulent modeling.

[2] In this work, agitation is preferred to mixing considering the fact that simulations are started with homogeneous suspension

1.2 Present Study

The focus of this investigation is to gain insight as to how non-Newtonian characteristics of the liquid phase affect the solid-liquid interaction of multi phase stirred tank flow. The non-Newtonian liquids considered here are the simplest and often encountered in oil sands tailings processing. Non-Newtonian behaviors described in this work are purely viscous in nature e.g. shear-thickening, shear-thinning with and without yield stress. Tailings (largely due to the fines) are known to exhibit these non-Newtonian characteristics and sometimes thixotropy; the added complexity of thixotropic rheology is beyond the scope of this work and hence not considered.

Together the clay and water phases of tailings can be modeled as a single homogeneous, non-settling carrier fluid [9]. The solids phase is treated as course monosized sand particles with size very typical of course particles found in tailings. The task of this research is to numerically simulate the agitation of tailings in a standard lab-scale tank equipped with baffles and a Rushton turbine. Given the dearth of literature on turbulent non-Newtonian stirred tank flow, the first stage of this work will aim at consolidating understanding of turbulent non-Newtonian single phase flow in stirred tank by DNS; and then after, in the second stage, particles will be added to the tank.

1.3 Outline of thesis

This thesis is structured in the order as indicated below:

Chapter 2 is a literature review highlighting the key concepts in this work, namely, turbulent stirred tank flow, turbulent non-Newtonian agitation and solid-liquid mixing.

Chapter 3 – methods and techniques – outlines the different non-Newtonian rheological models used in this work. The lattice-Boltzmann method is formally introduced. The numerical techniques involved in the implementation of some of

these models are discussed and afterwards 2D shear flows of these viscous non-Newtonian models are solved using the lattice-Boltzmann method. The analytical solution to these flows are also solved for and compared with simulation results.

Single phase non-Newtonian liquid agitation is presented in Chapter 4. This chapter will attempt to delve into qualitative and quantitative differences in turbulent structures like velocity structures, kinetic energy, anisotropy, viscosity, etc owing to non-Newtonian rheology. Results in this chapter will be analysed in several perspectives, as in light of theoretical, empirical and experimental work.

Chapter 5 will move one step up on Chapter 4 and address two-phase flows: particle distribution and settling in non-Newtonian liquids using the same tank settings and rheology in the previous chapter.

Then finally, Chapter 6 will reflect on the work as a whole: the perspectives gained and new research directions garnered from this work.

Bibliography

[1] Crowe, C., Sommerfeld, M., Tsuji, Y., "Multiphase Flows with Droplets and Particles", CRC Press LLC, 1998

[2] Ilea, C.G, Kosinski, P., Hoffmann, A.C., "3-D Eulerian-Lagrangian Simulation of Dust Lifting", International Conference of Numerical Analysis and Applied Mathematics, 2006

[3] Nijdam, J. J., Guo, B., Fletcher, D. F., Langrish, T.A.G, "Lagrangian and Eulerian Models for Simulating Turbulent Dispersion and Agglomeration of Droplets within a Spray", Third International Conference on CFD in the Minerals and Process Industries CSIRO, Melbourne, Australia, 2003

[4] Durst, F., Milojevic, D., Schonung, B., "Eulerian and Lagrangian Predictions of Particulate Two- Phase Flows: A Numerical Study", Appl. Math. Modeling, 8, 1984

[5] Hartmann, H., "Detailed Simulations of Liquid and Solid-Liquid Mixing: Turbulent agitated flow and mass transfer", Ph.D thesis, TU Delft, 2005

[6] Yu, H., Girimaji, S.S., Luo, L., "DNS and LES of decaying isotropic turbulence with and without frame rotation using lattice Boltzmann method" J. Comput. Phys., 209,2,2005

[7] Paul, E. L., Atiemo-Obeng, V., Kresta, S.M., "Handbook of Industrial Mixing", John Wiley & Sons, Inc., ISBN: 0-471-26919-0, 2004

[8] Venneker, B.C.H., Derksen, J.J., Van den Akker, H., "Turbulent non-Newtonian Flow in a Stirred Tank-LDA Experiments on the influence of Reynolds Number and Flow Index", Chemical Engineering Research and Design, Preprint, 2008

[9] Spelay, R.B., "Solids Transport in Laminar, Open Channel Flow of non-Newtonian Slurries", Ph.D. thesis, University of Saskatchewan, 2007

2 Literature Review

Most published research on agitation of solid suspensions in stirred tanks deal with Newtonian carrier phases. This comes as no surprise given the multi phase nature of the flow, complex flow structures in a stirred tank and variety of non-Newtonian characteristics. Consequently, in the literature, one finds studies on turbulently agitated solid suspensions (in Newtonian liquids) in one group, and more recently, studies on single phase non-Newtonian turbulently stirred tank flow in another group.

Possibly, Derksen's [1] study on solid particle mobility in turbulently agitated Bingham liquid is the only reported study of agitation of solid suspension in non-Newtonian carrier fluid. Pinelli and Magelli [2] carried out experiments to find out how particles settle in pseudoplastic liquids. Their interest in particle terminal settling velocities and dispersion coefficients limit their work to the laminar regime. Similarly, Roman and Tudose [3] studied the impact of Rushton turbine blade modification on particles suspended in five pseudoplastic liquids up to $\mathrm{Re} = 2400$. In their work nothing is mentioned about the impact of non-Newtonian fluid and no comparison is made to Newtonian systems.

In view of the fact that the literature on agitation of solid suspensions in stirred tank is vast, coupled with the dearth of cases using non-Newtonian carrier phase, this review will focus on three key areas. First, a dissection on flow structures in turbulent stirred tank flow with Rushton turbine, then followed by a review on turbulent non-Newtonian stirred tank agitation. The last segment of the review will be a paragraph discussing solid suspensions in stirred tanks.

2.1 Stirred tank flow with Rushton turbine

The advent of non-intrusive measuring techniques and technologies such as Laser Doppler Anemometry [4–6]; Particle Image Velocimetry [7–9], etc has enabled more accurate and extensive characterization of the flow structures in a stirred vessel. Previously, flow characterization was accessed indirectly by means of global parameters such as, power drawn by impeller, circulation times, pumping capacity, etc [10]. These "traditional" methods quickly phased out when more accurate description of the flow field was desired. Preceding intrusive techniques such as the hotwire anemometry (HWA), constant temperature anemometry (CTA) enabled velocity fluctuations at points in the flow to be measured. Although these techniques and their variants are still used today, the state of the art is non-intrusive optical techniques. As said previously, these new techniques can give detailed and full flow field information with remarkable accuracy.

A turbulent stirred tank flow is a complex multi-scale time-dependent flow; the largest scale being about the diameter of the impeller and smallest, obviously, the Kolmogorov scale. The rotating turbine generates several vortices and jets which interacts with the walls and baffles to create flow structures such as circulating loops, trailing vortices, etc. Tatterson [11] accounts for the various flow systems which can be found simultaneously in stirred tank flow; his account is elaborated by Venneker [12] who depicts these structures pictorially in his thesis. The points below are excerpted from Venneker's work:

1. Bulk flows – the bulk flows generated by a Rushton turbine generally prescripe the radial flow patterns prevailing in the tank. The observed flow patterns consist of two circulation loops located above and below the impeller disk axis. In a developed turbulent flow, large recirculation zones, toroidal vortices, and decaying vortex systems are some of the flow structures that can be associated to the bulk flows.

2. Impeller flows – flows under this category include: discharge from the impeller, the trailing vortices behind the impeller blades and blade wakes. These

flows are also distinctive in their high shear and high local velocities. It is possible (actually often encountered), computationally and also with experiments to achieve instantaneous velocities higher than impeller tip speed V_{tip} in these regions.

3. Wall flows – wall flows include impinging jets originating from the impeller and shed vortex systems which can be regarded prominent flows as well as minor flows likes corner flows and baffle bound flows.

The author urges readers interested in understanding the evolution and interaction between these flow groups to consult cited references.

2.2 Non-Newtonian stirred tank agitation

Studies of agitation of non-Newtonian liquids in stirred vessels dates back to the late 50's prominently with Metzner and Otto [13] who postulated the average shear rate concept for determining viscosity of non-Newtonian liquids. The linear relationship they proposed has been verified by [14, 15]. It has also been criticized in handful publications − with most critics concluding the average shear is reasonable only in the laminar regime and for low bottom impeller clearance. Skelland [16] also argues the concept leads to no unique power-curve [17]. Qualitative investigation into the flow pattern formed by a non-Newtonian fluid agitated with a Rushton turbine was first done by Metzner and Taylor [14]. Their conclusions though are valid for the laminar and early transition regime Re $\leq$ 450. Several studies that followed focused predominantly on effect of non-Newtonian rheology on power-consumption or different impeller types in the laminar regime [18–21].

Another important research area in agitation of non-Newtonian fluids in stirred tank is agitation of yield stress fluids such a Bingham or Herschel-Bulkley fluids. It is known that active mixing occurs within the caverns formed around the impeller during the agitation of such fluids; there has been several investigations into the cavern formation, factors that influence the size of the cavern [22–26].

The literature of turbulent non-Newtonian stirred tank flow is limited [16]. Hockey et al [27] identified that the flow field created by inelastic shear-thinning liquids are very similar to that of a Newtonian, however this similarity pattern in the turbulent regime was "less clear" [12] . The opposite effect is observed by Couerbe et al [28], who observed in the turbulent regime, the flow field of a thixotropic shear-thinning liquid with yield-stress is very much like the flow field of a Newtonian fluid. Finally, the time-dependent nature of thixotropic apparent viscosity has been analyzed by Derksen and Prashant [29] in a turbulently stirred tank equipped with a Rushton turbine. The build-up and break-down of scalar fluid network structure during agitation and influence of Deborah number (Db is the ratio of characteristic fluid time scale to a characteristic flow time) presents a complex and intriguing system. As per their findings, at Db=1, turbulently agitated thixotropic liquids are remarkably similar to time-independent liquids.

2.3 Solid suspension in stirred tanks with Newtonian liquids

Clearly, the local and global liquid flow in a stirred tank impact particle distribution and flow field. In practice, the goal of any solid-liquid mixing or agitation is to achieve a certain degree of homogeneity. A survey of the literature showed there exist three states of solid suspension: partial suspension, complete suspension and uniform suspension. The partial suspension state describes a state where solids settle at the bottom during agitation; the complete suspension state occurs when there is complete particle mobility and particles are seen suspended in the liquid and the uniform suspension describes a state of suspension where the particle concentration is uniform through vessel and further increment in stirrer speed does not enhance suspension quality [9]. In the literature, one finds that earlier (and majority) of research [30–40] into particle transport in turbulent stirred tanks focused on impeller speed, clearance or geometric configurations required for com-

plete suspensions [3]. As said previously, all these investigations were done in Newtonian carrier liquids; and mostly with heavy (non-floating) solids [41]. In non-Newtonian liquids however, some of these findings might not hold. For example, suspension homogeneity increases with increasing impeller speed for Newtonian suspensions; for suspensions with Bingham liquids, the opposite effect is observed [1].

Bibliography

[1] Derksen, J.J., "Solid Particle Mobility in agitated Bingham liquids" , Industrial & Engineering Chemistry Research, 48, p2266, 2009

[2] Pinelli, D., Magelli, F., "Solids settling velocity and distribution in slurry reactors with dilute pseudoplastic suspensions", Ind. Eng. Chem. Res., 40, p4456-4462, 2001

[3] Roman, R.V., Tudose, R.Z., "Studies on transfer processes in mixing vessels: effect of particles on gas-liquid mass transfer using modified Rushton turbine agitators", Chem. Eng. J. 61, 83-93, 1996

[4] Durst, F., Melling, A., Whitelaw, J. H., "Principles and Practice of Laser-Doppler Anemometry", Academic Press, 1976

[5] Drain, L. E., "The Laser Doppler Technique", Wiley, 1980

[6] Venneker, B.C.H., Derksen, J.J., Van den Akker, H., "Turbulent non-Newtonian Flow in a Stirred Tank-LDA Experiments on the influence of Reynolds Number and Flow Index", Chemical Engineering Research and Design, Preprint, 2008

[7] Lourenco, L. M., Krothopalli, A., Smith. C.A, "Particle image velocimetry, in Advances in Fluid Mechanics Measurements", Springer-Verlag, Berlin, p127, 1989

[8] Adrian, R. J., "Particle imaging techniques for experimental fluid mechanics", Annu. Rev. Fluid Mech., 23, 261–304, 1991

[9] Paul, E. L., Atiemo-Obeng, V., Kresta, S.M., "Handbook of Industrial Mixing", John Wiley & Sons, Inc., ISBN: 0-471-26919-0, 2004

[10] Alexopoulos, A.H., Maggioris, D., Kiparissedis, C., "CFD Analysis of Turbulence non-homogeneity in Mixing Vessels: A two-compartment model", Chem. Eng. Sci., 57, 1735 – 1752, 2002

[11] Tatterson, G., "Fluid Mixing and Gas Dispersion in Agitated Tanks", McGraw-Hill, New York p669–679, p208–213, 1991

[12] Venneker, B.C.H., "Turbulent Flow and Gas Dispersion in Stirred Tank with Pseudoplastic liquids", Ph.D Thesis, TU Delft, 1999

[13] Metzner, A. B., Otto, R. E., "Agitation of non-Newtonian fluids", AICHE J., 3, p3–10, 1957

[14] Metzner, A. B., Taylor, J. S., "Flow patterns in agitated vessels", AICHE Journal 6, 109, 1960

[15] Wichterle, K., Wein, O., "Threshold of mixing non-Newtonian fluids", Int. Chem. Eng., 21, 116–120, 1981

[16] Skelland, A. H. P., "Non-Newtonian flow and heat transfer", John Wiley & Sons, Inc, 1967

[17] Chhabra, R.P.,Richardson, J.F., "Non-Newtonian Flow and Applied Rheology", Butterworth-Heinemann, Oxford, p208–211, 1999

[18] Rieger, F., Novak, V., Havelkova, D., "Homogenization efficiency of helical of a ribbon agitators", Chem. Eng. J., 33, p143–150, 1986

[19] Brito-de la Fuente, E., Choplin, L., Tanguy, P. A., "Mixing with helical ribbons: effect of highly shear-thinning behavior and impeller selection", Trans. Inst. Chem. Eng., 75, p45–52, 1997

[20] Ulbrecht, J.J., Carreau, P.J., "Mixing of viscous non-Newtonian liquids, in: J.J. Ulbrecht, G.R. Patterson (Eds.), Mixing of Liquids by Mechanical Agitation", vol. 1, Gordon and Beach, New York, USA, p 93–137, 1985

[21] Patterson, N.I., Carreau,P.J.,Yap, C.Y., "Mixing with helical-ribbon agitators. II. Newtonian fluids", Am. Inst. Chem. Eng. J. 25, p 508–515, 1979

[22] Amanullah, A., Hjorth, S. J., Nienow, A. W., "A new mathematical model to predict cavern diameters in highly shear thinning, power law liquids using axial flow impellers", Chem. Eng. Sci., 53, p455–469, 1998

[23] Elson, T. P., "Mixing of fluids possessing a yield stress", Proc 6th European Conference on Mixing, p485–492, 1988

[24] Elson, T. P., Cheesman, D. J., "Nienow, A. W., X-ray studies of cavern sizes and mixing performance with fluids possessing a yield stress", Chem. Eng. Sci., 41, 2555–2562, 1986

[25] Hirata, Y., Nienow, A. W., Moore, I. P.T., "Estimation of cavern sizes in a shear-thinning plastic fluid agitated by a Rushton turbine based on LDA measurements", J. Chem. Eng. Jpn., 27, p235–237, 1994

[26] Jaworski, Z., Pacek, A. W., Nienow, A. W., "On the flow close to cavern bound aries in yield stress fluids", Chem. Eng. Sci., 49, p3321–3324, 1994

[27] Hockey, R.M., Nouri, J.M., Pinho, F.T., Flow visualization of Newtonian and non-Newtonian fluids in stirred reactors, In Int. Symp. Flow Visualization V, p. 976-987,1989

[28] Couerbe, G., Fletcher, D. F., Xuereb, C., Poux, M., "Impact of thixotropy on flow patterns induced in a stirred tank: Numerical and experimental studies", Chemical Engineering Research & Design, 86, p545-553, 2008

[29] Derksen, J.J., Prashant, "Simulations of Complex flow of Thixotropic liquids", J. Non-Newtonian Mech., corrected proof, 2009

[30] Bakker, A., Fasano, J.B., Myers. K.J., "Effect of flow pattern on solids distribution in a stirred tank", Inst. Chem. Eng. Symp. Ser., 136, 65–72, 1994

[31] Baresi, A., Baldi, G., "Solid Dispersion in an Agitated Vessel", Chem. Eng. Sci. 42 (12), 2949-2956, 1987

[32] Nienow, A. W.,Miles, D., "The effect of impeller/tank configurations on fluid–particle mass transfer", Chem. Eng. J., 15, 13, 1978

[33] Nienow, A. W., "Suspension of solid particles in turbine-agitated baffled vessels", Chem. Eng. Sci., 23, 1453, 1968

[34] Baldi, G., Conti, R., Alaria, E., "Complete suspension of particles in mechanically agitated vessels", Chem. Eng. Sci., 33, 21, 1978

[35] Zwietering, T. N., "Suspending of solid particles in liquid by agitators", Chem. Eng. Sci., 8, 244, 1958

[36] Chapman, C. M., Nienow, A. W., Cooke, M., "Particle–gas–liquid mixing in stirred vessels: 1. Particle–liquid mixing", Chem. Eng. Res. Dev., 61, 71–81,1983

[37] Raghava Rao, K. S. M. S., Rewatkar, V. B., Joshi, J. B., "Critical impeller speed for solid suspension in mechanically agitated contactors", AIChE J., 34(8), 1332, 1988

[38] Rieger, F., Ditl, P., "Suspension of Solid Particles", Chem. Eng. Sci., 49(14), 2219–2227, 1994

[39] Choudhury, N. H., "Improved predictive methods for solids suspension in agitated vessels at high solids loadings, Ph.D. dissertation, University of Arkansas, AR, 1997

[40] Rieger, F., Ditl, P., Havelková, O., Proceedings of the Sixth European Conference on Mixing Pavia, Italy, pp. 251–258, 1988

[41] Hemrajani, R.R., Smith, D.L., Koros, R.M., Tarmy, B.L., "Suspending Floating Solids in Stirred Tanks-Mixer Design, Scale-Up and Optimization", 6th European Conference on Mixing, Pavia, Italy, 1988

3 Methods and Techniques

3.1 Viscous homogeneous fluid models

A fluid is a substance that continuously deforms so long as a deformation force is applied. When a fluid is showing uniform density, it is said to be homogeneous in its constitution. A homogeneous fluid is naturally incompressible given the fact that the absence of volume dilation or compression guarantees constant density and the density of a fluid is given in terms of its mass divided by volume. A viscous fluid is characterized by its viscosity – which is a measure of the fluid's internal resistance to deformation forces. In general, fluids are classified as Newtonian and non-Newtonian. For a Newtonian fluid, the applied stress is proportional to the instantaneous rate of shear and the constant of proportionality is its viscosity (also known as the dynamic viscosity). For non-Newtonian fluid, the viscosity is not constant as it may be a function of the shear rate as in power-law liquids, or the kinematic shear history as fluids showing thixotropy and/or elastic recovery [1]. According to the so-called generalized Newtonian model [2], the incompressible stress tensor is given as:

$$\tau_{ij} = -\eta S_{ij}; \qquad \eta = \eta(\dot{\gamma}) \tag{3.1}$$

Where $\eta(\dot{\gamma})$ is the shear-rate dependent viscosity; the shear rate $\dot{\gamma}$ is also determined from the second invariant of the rate-of-strain tensor $S_{ij} = \frac{1}{2}\left(\frac{du_i}{dx_j} + \frac{du_j}{dx_i}\right)$, this relation is given by (3.2) below with summation over

repeated indices:

$$\dot{\gamma} = \sqrt{2S_{ij}S_{ij}} \tag{3.2}$$

Note that for Newtonian fluids there is no shear rate dependency. However, for non-Newtonian fluids, the simplest empiricism for is the Ostwald de Waele's [3] power law expression.

$$\eta = K\dot{\gamma}^{n-1} \tag{3.3}$$

When deviations in using the power-law expressions are significant e.g. at low shear rates or very high shear rates, other fluid models such as the Carreau model which is a four-parameter model or the Ellis model (three parameter) or the Cross model (four parameter) is used. The Carreau model is given as:

$$\frac{\eta - \eta_\infty}{\eta - \eta_0} = (1 + (\lambda\dot{\gamma})^2)^{(n-1)/2} \tag{3.4}$$

where η_0, η_∞ are the zero shear and infinite shear viscosities respectively.

The Cross model is given by:

$$\frac{\eta - \eta_\infty}{\eta - \eta_0} = \frac{1}{1 + K(\dot{\gamma})^n} \tag{3.5}$$

The Ellis model which is three parameter unlike the two previous is:

$$\eta = \frac{\eta_0}{1 + (\tau/\tau_{1/2})^{\alpha-1}} \tag{3.6}$$

where η_0 is the zero-shear viscosity, α is a measure of shear-thinning index and $\tau_{1/2}$ is the shear-stress value when the apparent viscosity has dropped to half of η_0.

For fluids possessing yield stress, the Bingham (BH) and Herschel-Bulkley(HB) fluid models are often used. HB models are used to account for a fluid which exhibits shear-thinning behavior if the applied stress exceeds the yield stress; this is given by:

$$\begin{aligned} \eta &= \tau_0/\dot{\gamma} + K\dot{\gamma}^{n-1} \qquad |\tau| > \tau_0 \\ \eta &= \eta_0 \qquad\qquad\qquad\quad |\tau| \leq \tau_0 \end{aligned} \tag{3.7}$$

where τ_0 is the yield stress and $|\tau|$ is the norm of the shear-stress expressed as $|\tau| \equiv \sqrt{\frac{1}{2}\tau_{ij} : \tau_{ij}}$ summing over repeated indices. When a fluid exhibits a uniform viscosity if the yield stress is exceeded, then the BH model suites this fluid model. As like the HB model, the unyielded BH liquid is characterized by the zero-shear viscosity η_0 and the viscous behavior after yielding is given by:

$$\eta = \tau_0/\dot{\gamma} + K \qquad |\tau| > \tau_0 \tag{3.8}$$

Fig. 3.1, shown below, is a rheogram for the fluid behaviors discussed above. Pseudoplastic and dilatant refers to shear-thinning and shear-thickening fluids respectively likewise the HB fluid is called pseudoplastic with yield point. Fig.3.1b shows the typical viscosity response to shearing for these fluids.

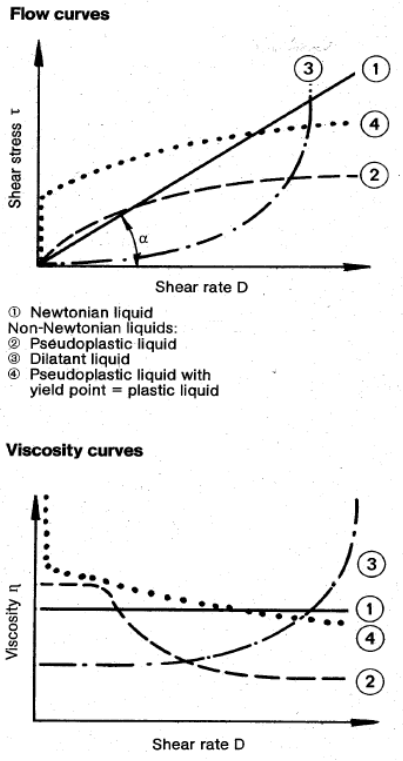

Figure 3.1: Rheograms of common fluids. Source: Schram [4]

3.2 The lattice-Boltzmann method

The lattice Boltzmann method LBM is numerical scheme for solving the incompressible Navier-Stokes equation. Basically, the LBM simulates the macroscopic fluid dynamics as a many discrete microscopic particles which obey the conservation principles [5]; in this way the macroscopic dynamics become sensitive to the "underlying details of microscopic physics" [6]. The LBM solves directly the lattice-Boltzmann equation which describes the ensemble average kinetics of particles moving along the edges of a lattice. In principle, the LBM provides explicit solution to the discrete form of the Boltzmann equation. The method is second order accurate in both space and time in spite of the fact that the scheme – eqn (3.9) – is first order discretized. The two- and three- dimensional projections of the face centred hypercubic (FCHC) lattice is commonly used in solving the Navier-Stokes equation [7,8]. The LBM lattice employed throughout this thesis is a regular cubic lattice having eighteen velocity directions – this model is sometimes referred to as the D3Q18 model and its shown in fig. 3.2.

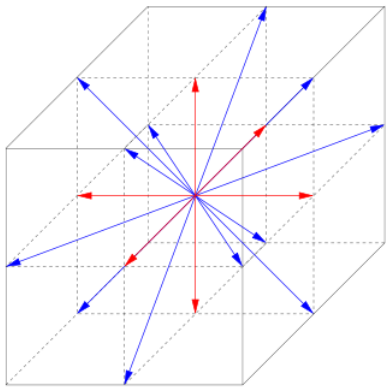

Figure 3.2: The D3Q18 LBM model showing the 18 velocity directions $\mathbf{c}_i$; vectors in red have multiplicities $m_i = 2$ while those in blue have $m_i = 1$. Source [9]

Somers [10] provides an elaborate scheme for solving the lattice-Boltzmann equation as:

$$N_i(x + \mathbf{c}_i, t + 1) = N_i(x, t) + \Gamma_i(N) \tag{3.9}$$

Where Γ_i is the non-linear collision operator which has the following properties:

$$\sum_i \Gamma_i(N) = 0; \qquad \sum_i \mathbf{c}_i \Gamma_i(N) = \mathbf{f} \tag{3.10}$$

If the right choice of Γ_i is made then, the scheme converges towards the equilibrium solution of:

$$N_i = \frac{m_i \rho}{24}\left(1 + 2\mathbf{c}_i \cdot \mathbf{u} + 3\left[\mathbf{c}_i\mathbf{c}_i : \mathbf{u}\mathbf{u} - \frac{1}{2}\mathrm{tr}(\mathbf{u}\mathbf{u})\right] - 6\nu\left[(\mathbf{c}_i\nabla)(\mathrm{c}_i \cdot \mathbf{u}) - \frac{1}{2}\nabla \cdot \mathbf{u}\right]\right) \tag{3.11}$$

The conservation equations can be derived from these equations as follows: Substituting (3.11) in (3.9) and a summation over i followed by the application of (3.10a) yields the equation for the conservation of mass $\frac{\partial \rho}{\partial t} + \nabla \cdot \rho\mathbf{u} = 0$.
Similarly, the conservation of momentum is recovered when (3.9) is multiplied by $\mathbf{c}_i$ and (3.11) is substituted into the derived expression. A summation over i, and applying (3.10b) yields the regular Navier-Stokes equation in the limit of incompressibility.

$$\frac{\partial \rho\mathbf{u}}{\partial t} + \nabla \cdot \rho\mathbf{u}\mathbf{u} = -\nabla P + \nabla \cdot \rho\nu[\nabla\mathbf{u} + (\nabla\mathbf{u})^T] - \nabla\left(\frac{1}{2}\rho\nu\nabla \cdot \mathbf{u}\right) + \mathbf{f}$$

In the evolution of the scheme described above by Eggels and Sommers [6], two steps can be distinguished. A propagation step, in which mass density $\mathbf{N_i}$ at lattice node $\mathbf{x}$ is "shuffled" to position $\mathbf{x} + \mathbf{c}_i$; in the next step, the collision step, $\mathbf{N_i}$ is "redistributed" in all i directions to each grid point. In either steps, boundary conditions − no-slip (bounce-back), free-slip, periodic etc. − can be implemented; this could be done by imposing rules regarding movements of mass densities in the propagation step or velocities can be prescribed in certain regions in the flow as employed by Derksen and Van den Akker [8] in the simulation of stirred tank flow. Please refer to the cited article for details on the adaptive force-field technique

employed in imposing liquid velocities on the rotating impeller and static tank wall.

The greatest advantage of the LBM is in its efficiency. Compared to other second-order numerical schemes, the LBM works much faster in terms of simulation time per grid node per time step. As an example, the LBM was found to be 500-600 times faster than the FLUENT code (a finite volume method) in a comparative numerical study on laminar flow in a Kenics static mixer [11]. The efficiency of the LBM is further as a result of three features of the method: first, the LBM employs simple kinetic equations unlike other schemes which discretize the Navier-Stokes equation. Second, the LBM computations are fully parallel i.e. same computations are made on each grid site. And finally, operations in LBM are local since only neighboring particles interact. Another advantage of the LBM is its flexibility with respect to complex boundaries implementation. The adaptive force-field technique was used to implement stirred tank and impeller geometry without loss to the efficiency of the method.

The disadvantage of the LBM is the fact that it is generally restricted to incompressible flows. However this restriction will be a thing of the past in the near future as recent studies [12] have explored higher Mach number possibilities to simulate compressible flows.

3.3 Non-Newtonian viscosity implementation and verification in LBM

3.3.1 Power-law liquids

Since the LBM works more efficiently in cubic domains and with constant fluid viscosity, any other rheological model passed to it must first be tested with simple cases to validate its accuracy. In this section 2D laminar cases are passed to the solver and the results are compared with analytical solution. A simple channel flow driven by a constant body force can serve this purpose; in this flow scenario

the (incompressible) equations of motion are given by:

$$\rho \frac{D\mathbf{v}}{Dt} = -\nabla p - [\nabla \cdot \boldsymbol{\tau}] + \rho \cdot \mathbf{g} + \mathbf{f} \tag{3.12}$$

$$\frac{\partial u}{\partial x} + \frac{\partial v}{\partial y} = 0 \tag{3.13}$$

Expanding (3.12) in x,y coordinates axis

$$\rho \left(\frac{\partial u}{\partial t} + u\frac{\partial u}{\partial x} + v\frac{\partial u}{\partial y} \right) = -\frac{\partial p}{\partial x} - \left[\frac{\partial \tau_{xx}}{\partial x} + \frac{\partial \tau_{yx}}{\partial y} \right] + \rho \cdot g_x + f_x \tag{3.14}$$

$$\rho \left(\frac{\partial v}{\partial t} + u\frac{\partial v}{\partial x} + v\frac{\partial v}{\partial y} \right) = -\frac{\partial p}{\partial y} - \left[\frac{\partial \tau_{xy}}{\partial x} + \frac{\partial \tau_{yy}}{\partial y} \right] + \rho \cdot g_y + f_y \tag{3.15}$$

Assuming further that:

- steady states
- no pressure gradients
- parallel flow i.e. $v = 0$
- gravity in z-direction only
- body force in streamwise x-direction only, thus, $f_y = 0$ and $f_x = f_0$

Under these assumptions (3.13) reduces to

$$\frac{\partial u}{\partial x} = 0 \tag{3.16}$$

and the Navier-Stokes eqns (3.14)-(3.15) become

$$0 = -\frac{\partial \tau_{yx}}{\partial y} + f_0 \tag{3.17}$$

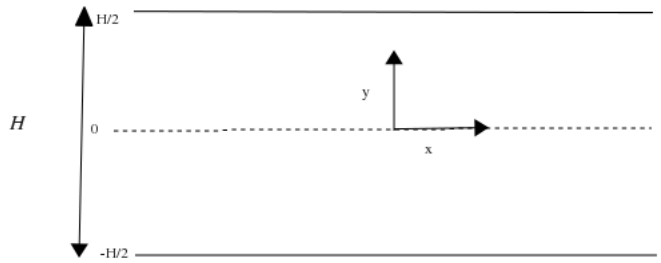

Figure 3.3: schematic of the 2D planar flow driven by body force(f_0)

Solving for $u(y)$between $0 \leq y \leq \frac{H}{2}$ (since solution as well as the flow is symmetrical) and invoking the power-law expression (3.3) $f_0 = \frac{d\left(K(-\frac{du}{dy})^n\right)}{dy}$ this yields

$$u(y) = \left(\frac{f_0 \cdot H}{K}\right)^{1/n} \frac{H}{(1+1/n)} \left[1 - (y/H)^{1+1/n}\right] \tag{3.18}$$

3.3.2 Viscous models for HB and BH fluids

In the implementation of BH and HB models, the method of Beverly & Tanner [13] was used. Basically, at shear rates below a critical shear rateγ_c the fluid is assigned a high but not infinite viscosity η_r(zero shear viscosity); and above this critical shear rate the fluid yields and with an apparent viscosity deduced from the slope of the profiles; mathematically, the relation between the critical shear rate and viscosities is given as: $\dot{\gamma}_c \equiv \frac{\tau_0}{\eta_r - \eta}$ this is illustrated from fig. 3.4.

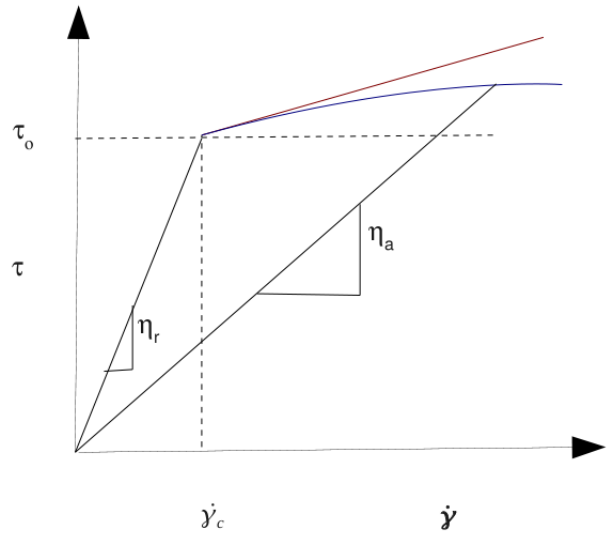

Figure 3.4: The viscous behavior of HB and BH models in the simulation. Observe the curve line (in blue) is the response for the HB model and the solid line in red above is the BH response. The slope of the straight line that touches the HB curves gives the the apparent viscosity of the fluid. For the BH fluid the apparent viscosity is the slope of the from origin that touches the BH profile.

Formally, the HB rheological model is represented as:

$$\begin{aligned} \tau_{ij} &= 2(\tau_0/\dot{\gamma} + K\dot{\gamma}^{n-1})S_{ij} \qquad \text{if} \quad |\tau| > \tau_0 \\ S_{ij} &= 0 \qquad \text{if} \quad |\tau| \leq \tau_0 \end{aligned} \tag{3.19}$$

The expression for its viscosity thus becomes:

$$\begin{aligned} \eta_a &= \tau_0/\dot{\gamma} + K\dot{\gamma}^{n-1} \qquad \text{if} \quad |\tau| > \tau_0 \\ \eta &= \eta_r \qquad \text{if} \quad |\tau| \leq \tau_0 \end{aligned} \tag{3.20}$$

eqn(3.19) and (3.20) are also valid for the BH model when $n = 1$. In the derivation of the analytical solution for the planar 2D flow of HB liquid, (3.19) is inserted into the (3.18) and the resultant equation is integrated with respect to y giving:

$$u(y) = \frac{n\,(f_0/K)^{1/n}}{n+1}\left((H - \tau_0/f_0)^{1+1/n} - (y - \tau_0/f_0)^{1+1/n}\right) \tag{3.21}$$

for $0 < y < y_1$ where y_1 is the width of the yielded region. In the plug flow (un-

yielded) region in the center where velocity is maximum, the expression becomes $u(y) = u_{max} = \frac{n(f_0/K)^{1/n}}{n+1}(0.5H)^{1+1/n}$ and this occurs at $y_1 < y < \frac{1}{2}H$.

3.3.3 Lattice-Boltzmann simulation of laminar 2D non-Newtonian shear flows

In the simulation of laminar 2D plane flow, an in-house LBM flow solver for 3D channel flow was used. The original code was made 2D by altering the boundary conditions so that the previous $40 \times 21 \times 21$ grid size was now 40×21; a temporal size 10^5 was long enough for flow to reach steady states. The Reynolds number for the flows were defined as:

$$Re = \frac{\rho_l u_{max} H}{\eta_a} \tag{3.22}$$

where u_{max} is the characteristic velocity, which is actually the maximum velocity derived in the analycial solution $u_{max} = \frac{n(f_0/K)^{1/n}}{n+1}(0.5H)^{1+1/n}$. For power-law liquids, the introduction of eqn (3.3) into the (3.22) simplifies further to

$$Re = \frac{\rho_l u_{max} H}{K\dot{\gamma}^{n-1}} = \frac{\rho_l u_{max} H}{K(u_{max}/H)^{n-1}} = \frac{\rho_l u_{max}^{2-n} H^{n-2}}{K}$$

so in effect for these cases, there are n, K, f_0, H and ρ_l in the parameter space. n is chosen, e.g. in the power-law cases $n = 0.68$ and $n = 1.20$ for the shear-thinning and shear-thickening respectively. Also in the power-law cases, f_0 and K are chosen carefully in a way such that when u_{max} is determined its value will not to achieve $|\mathbf{u}| \geq 0.2$ lattice units; an absolute velocity beyond this value causes the LBM to breakdown in the simulation. H is known from grid size specification in our code, ρ_l is also known a priori since it has a constant value in LBM. Given that, Re and η_a comes out from eqn (3.22) and (3.3) respectively. In HB simulation, the parameter space becomes larger with addition of η_r. The value of η_r is usually chosen in the range $0.1 - 0.25$ and η_a is normally expected to be at least 150 times less η_r (see the article by Beverly & Tanner [13]). Also a few derived quantities are added such as: $\tau_0 = f_0 \cdot \frac{H}{4}$ (the choice of $H/4$ is to force the plug flow region to occupy exactly

half of the flow width), and $\dot{\gamma}_c = \frac{\tau_0}{\eta_r - \eta_a}$. With τ_0 now found, η_a in eqn(3.20) can be calculated, since n is also known a priori and $\dot{\gamma}$ in eqn (3.19) can be calculated from u_{max} and H as done for the power-law liquids.

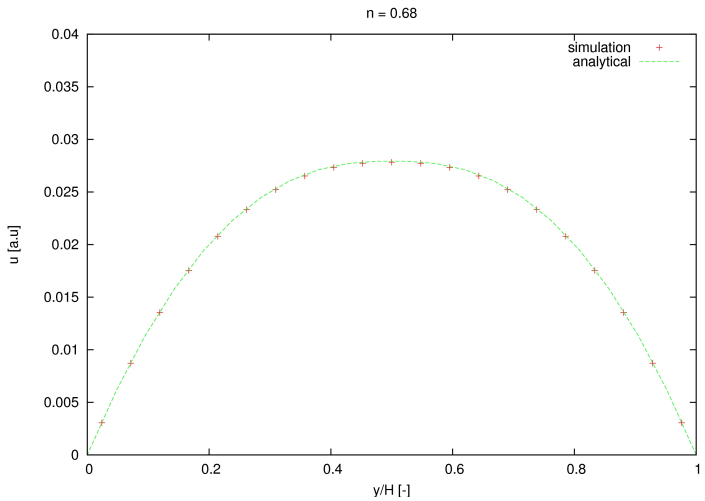

Figure 3.5: Comparison of the simulation and analytical solution derived for the power-law fluid; for this particular flow Re=95 and n=0.68. Maximum deviation computed was 0.92%

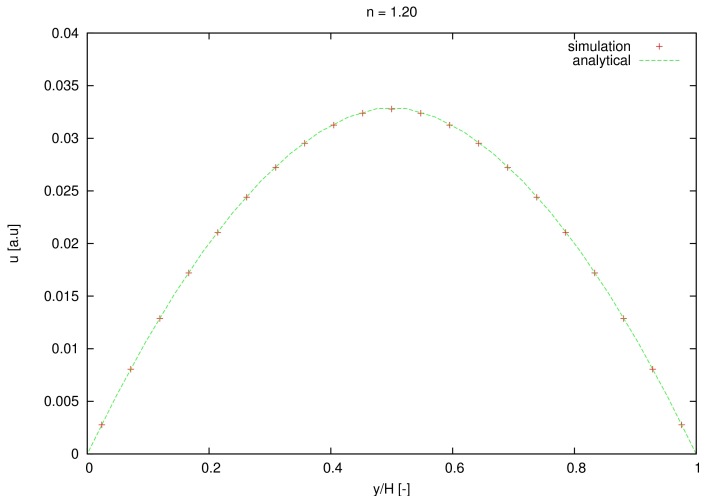

Figure 3.6: Comparison of the simulation and analytical solution derived for the power-law fluid; for this particular flow Re=95 and n=1.20. Maximum deviation computed was 1.01%

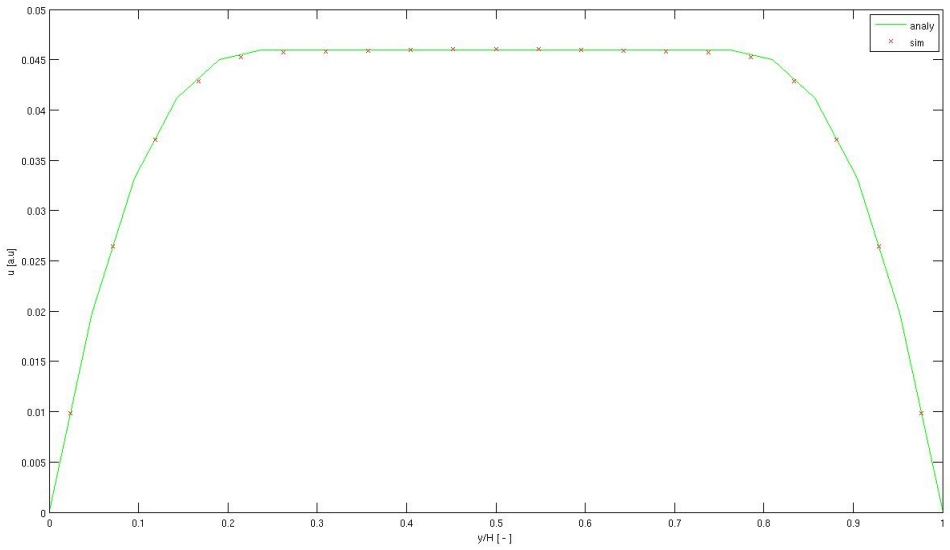

Figure 3.7: Comparison of the simulation and analytical solution derived for the HB fluid; for this particular flow Re=165 and n=0.60. Maximum deviations were found to be 2.4% (at the edges of plug region).

3.4 Remarks on 2D planar flows

In general the figures show good agreement between simulation and analytical solutions. The simulations of power-law liquids, for as many cases of different n and Re passed to the solver, error margins less than 1% throughout profile length was recorded. Flows with yield stress liquids were engineered such that the middle plug flow region occupied the mid-half of the flow width. For these liquids, high ($> 1\%$) deviations are seen in the regions just bordering the plug flow. It was found out that the by tuning the ratio of η_r to be two orders of magnitude η_a these regions could be somewhat "stabilized" and hence reduce the margin of error. In the opinion of the author, the error of 2.4% at these edges should be accepted given the fact that the simulation clearly captures the flow profile and gives less than 2.4% error in other parts of the profile.

3.5 Summary and Outlook

A scheme by Eggels & Somers [7] for solving the incompressible Navier-Stokes equation using the LBM has been presented. The scheme is numerically efficient and requires moderate computational resources to resolve even high Re flows. Although it works very well in uniform cubic grids, it can be adapted to complex geometries provided higher interpolation methods are used [8]. This will be evident in subsequent chapters which deal with stirred tank geometries. Rheological models for non-Newtonian behavior presented, are the simplest and commonly encountered non-Newtonian liquids in oil sands tailings operations. The implementation of these non-Newtonian models into LBM was straight forward and proved the LBM as an efficient flow solver. When compared with exact solution, deviations of no more than 2.4% were realized. In later chapters, these rheologies (with and without solids) will be agitated in stirred tank and examined qualitatively and quantitatively.

Bibliography

[1] Chhabra, R.P., Richardson, J.F., "Non-Newtonian Flow and Applied Rheology", Butterworth-Heinemann, Oxford, pp. 208–211, 1999

[2] Bird, R.B., Stewart, W.E., Lightfoot, E.N., "Transport Phenomena", John Wiley & Sons Inc., 2nd Edition, pp. 240-243, 2002

[3] Ostwald, W., Kolloid-Zeitschrift, 36,99-117, 1925; Waele, A. de., Oil Color Chem. Assoc. J., 6, 33-88, 1923

[4] Schramm, G., Introduction to Practical Viscometry, HAAKE publications, 1981

[5] Frisch, U., Hasslacher, B., Pomeau, Y., "Lattice gas automata for the Navier-Stokes equation", Phys. Rev. Lett. 56 (14), 1505, 1986

[6] Chen, S., Doolen, D.G., "Lattice Boltzmann Method for Fluid Flow", Ann Rev Fluid Mech, 30, 329, 1998

[7] Eggels, J.G.M.; Sommers, J.A., "Numerical Simulation of Free Convective Flow Using the Lattice Boltzmann Scheme", Int. J. Heat Fluid Flow, 16, 357 ,1995

[8] Derksen, J. J., Van den Akker,H. E. A., "Large Eddy Simulations on the Flow Driven by a Rushton Turbine", AIChE J., 45(2)209., 1999

[9] Stallkamp, J., Lattice-Boltzmann Simulations of Colloids in Hydrodynamic Fields, University of Bielefeld, Diploma thesis, 2003

[10] Somers, J. A., "Direct Simulation of Fluid Flow with Cellular Automata and the Lattice-Boltzmann Equation", Appl. Sci. Res., 51, 127, 1993

[11] Rhode, M. Extending the lattice-Boltzmann method: Novel techniques for local grid refinement and boundary conditions, PhD Thesis, TU Delft, 2002

[12] Alexander, F.J., Chen, H., Doolen, D.G., Lattice Boltzmann model for compressible fluids. Phys. Rev. A, 46(4):1967–1970, 1992

[13] Beverly, C. R., Tanner, R. I., "Numerical Analysis of Extrudate Swell in Viscoelastic Materials with yield Stress", J. Rheology, 33, 989,1989

4 Single Phase non-Newtonian Turbulent Stirred tank Flow

In this chapter, results and analysis of turbulent stirred tank flow for single phase non-Newtonian – shear-thinning, shear-thickening, and Bingham – fluids are presented. An additional Newtonian case is simulated for comparison. The outline of this chapter is as follows: First, an analysis of turbulent structures in terms of velocity, kinetic energy and anisotropy. This is followed by a comparison of average velocity field data of shear-thinning liquids to empirical correlations in the literature. Finally, the power number of the various flows will be computed from the simulations and compared with data in the literature.

4.1 Fluid characteristics

In developing rheological models for shear-thinning/thickening fluids, a method similar to the one used by Metzner & Otto [1] was considered. An apparent instead of "average" shear rate based on the impeller tip speed was employed; the derivation of $\dot{\gamma}_a = V_{tip}/D$ closely resemble the approach by Wu et al [2] although $V_{tip} = \Omega\frac{D}{2} = \pi ND$ is employed here rather than average velocity. With the value of $\dot{\gamma}_a$ in place, the apparent viscosity $\eta_a = K{\dot{\gamma}_a}^{n-1}$ in the power-law [3] can be deduced from the relation since K and n are characteristics of the fluid. For the Bingham liquid, the method of Beverly & Tanner [4] was followed; in this method, the fluid behaves as a highly viscous fluid below a critical strain rate and above this critical strain rate, the fluid "yields" with its apparent viscosity given by:

$\eta_a = \tau_0/\dot{\gamma} + K$. Please refer to the previous chapter for details. In the base cases– shear-thinning($n = 0.5$), shear-thickening($n = 1.5$), Newtonian and Bingham– the flows are desired to have Re=6×10^3, defining Re based on the impeller as:

$$Re = \frac{\rho_l N D^2}{\eta_a} \tag{4.1}$$

Note that in the case of the Newtonian fluid the apparent viscosity $\eta_a = \mu$, and for the Bingham(BH) fluids is equal to the slope of the line as illustrated in chapter 3 of this thesis. Eqn (4.1) presents four degrees of freedom, and in the simulation as a whole, there exist five degrees of freedom with respect to parameter space - $-n, N, K, D, \rho_l$. The stirred tank to be simulated is a cylindrical tank of volume 10L (see next section below on dimensions), given that D comes automatically from tank dimensions, ρ_l like Re and n are known a priori. N is chosen such that $V_{tip} \leq 0.2$ lattice units; in base cases for example where $N = 10$rev/s corresponds to $\Omega = 2\pi/2000$ in the simulation and thus $V_{tip} = 0.0946$ lattice units. With N, η_a can be deduced from 4.1. n, flow indices in this work are taken from similar studies in the literature and thus, K can be back calculated from η_a only. In the Bingham case, the yield stress and associated viscosity modeling present extra parameters and quantities i.e. $\tau_0, \dot{\gamma}_c, \eta_r$. As such another dimensionless number is defined to cater for these parameters. A yield-stress number $Y = \frac{\tau_0}{\rho_l N^2 D^2}$, defined as ratio of yield stress to inertial stresses, is calculated for the liquid in the stirred tank and instantiated in the simulation as well. With τ_0 found, $\dot{\gamma}_c \equiv \tau_0/\eta_r$ as η_r is always chosen in the order of $\eta_r \geq 10^2 \eta_a$.

Rheology	$\eta_a\ [kg/m/s]$	$K[kg/m/s^n]$	$n[-]$	$Y(\tau_0)$
Newtonian	1.014×10^{-2}	-	-	-
Bingham	1.014×10^{-2}	1.014×10^{-2}	-	$2.18 \times 10^{-2}(12.67Pa)$
shear-thinning	1.014×10^{-2}	5.68×10^{-2}	0.5	-
shear-thickening	1.014×10^{-2}	1.844×10^{-3}	1.5	-

Table 4.1: viscous properties of liquids model led in base case simulation. All liquids in this work have $\rho_l = 10^3 kg/m^3$

4.1.1 Stirred tank geometry

The agitation system employed is a standard 10L mixing tank with diameter $T = 0.234m$. It is equipped with a Rushton turbine (6-blade) impeller of diameter $T/3$ and mounted at clearance $T/3$. Baffles are mounted vertically on the inside cylindrical walls to prevent solid body rotation of the fluid and inhibit surface vortex formation. See Fig. 1 below for more details. Note that the top of the tank is closed, this ensures Froude and Weber number effects are absent; also, a hole is made in the lid to tightly fit the top of the impeller shaft. The impeller in base case simulations spins with a speed of 10rev/s.

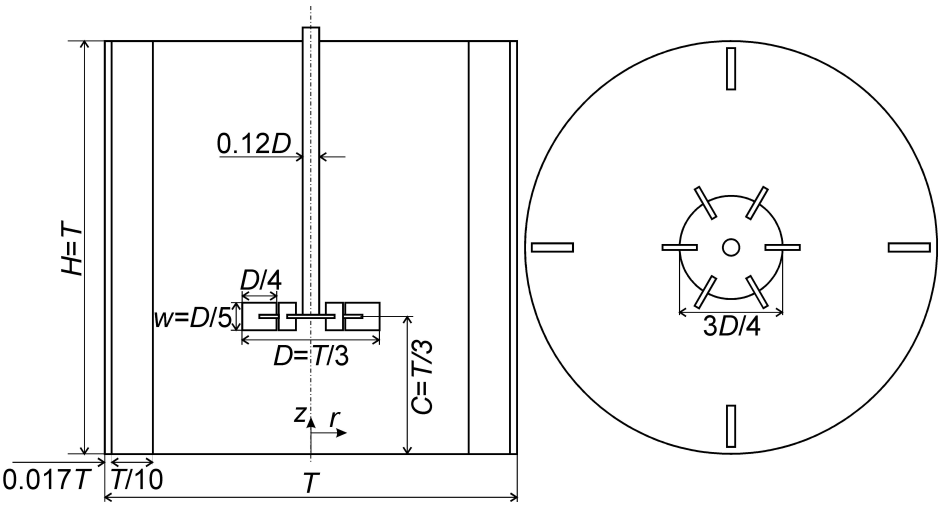

Figure 4.1: Tank geometry; midway view of the tank (left) and vertical cross-section view at z=T/3 in (r,z) co-ordinates. Source: [5]

4.1.2 Simulation Procedure

The lattice-Boltzmann method is employed in solving the equations of motion. The high numerical efficiency of the method enables highly resolved flows of high Reynolds numbers. In the simulation set-up a grid of size 180^3 is chosen as domain size. On each grid node, 21(18 LBM directions + 3 force components) single-precision, real values (4 bytes each) have to be stored; thus, each simulation occupies $180^3 \times 21 \times 4 \approx 0.5$gigabyte of memory. All simulations were run on (the

neskerd)[1] PC cluster with Dual Quad-core AMD Opteron(tm) 1895 MHz processor which has 8 nodes of combined physical memory 16.5gigabyte. The rotation of the impeller was modeled by adaptive force-field technique [6] based on earlier work by Goldstein et al [7]. The impeller makes a complete revolution in 2000 time steps, thus, 1 time step on the simulation is $(2000N)^{-1} = 50\mu S$ on the wall clock. The flow field is initialized to zero at start. The flow becomes more or less steady after 20 impeller revolutions; this was monitored by observing the velocity time series at a point below the impeller $(z/T = 0.11)$. Then after, 10 or 15 impeller revolutions more were preformed for the phase-averaged angle resolved data to be processed. Running four cases in the base case simulations on four cluster nodes at a time, it took between 14-18days to complete with the Newtonian case always being first to complete.

4.2 Results and Discussion

4.2.1 Velocity snapshots

Simulations in the base cases were done for a total of 30 impeller revolutions. As evident in the time series fig. 4.2 start-up phase behavior was lost before $tN = 10$. Nevertheless, the instantaneous velocity snapshots, fig.4.3a-d show it took about 5 revolutions more to stir up the full flow field and turbulent eddies can be seen in the flow fields of Newtonian, shear-thinning and shear-thickening at $tN = 20$ and beyond.

[1] stationed in the CME building of University of Alberta

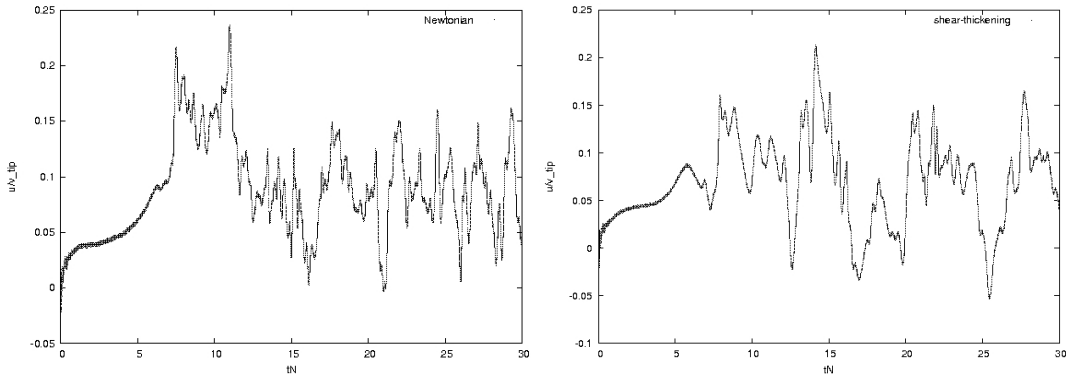

Figure 4.2: Time series profiles for base cases Newtonian and shear-thickening $n = 1.50$ monitored at the point located in the center (radial location $2r/D = 0$) of mid-baffle plane at $z/T = 0.11$

Notice the cavern like structure around the impeller of the shear-thinning fluid, this is not very clear and will be dissected later in the discussion. For the Bingham fluid simulation, the development of the cavity (as a full dome) shows up at $tN = 5$, however, inside the cavity the flow structures are not laminar given the absence of left-right symmetry; thus the flow immediatedly around the impeller outflow and regions near the "cavity" is best said to be in the transition regime. The entire flow is largely laminar in view of the fact that the cavity occupies only a small volume of the tank and also in the regions outside the cavity the Bingham liquid is stationary.

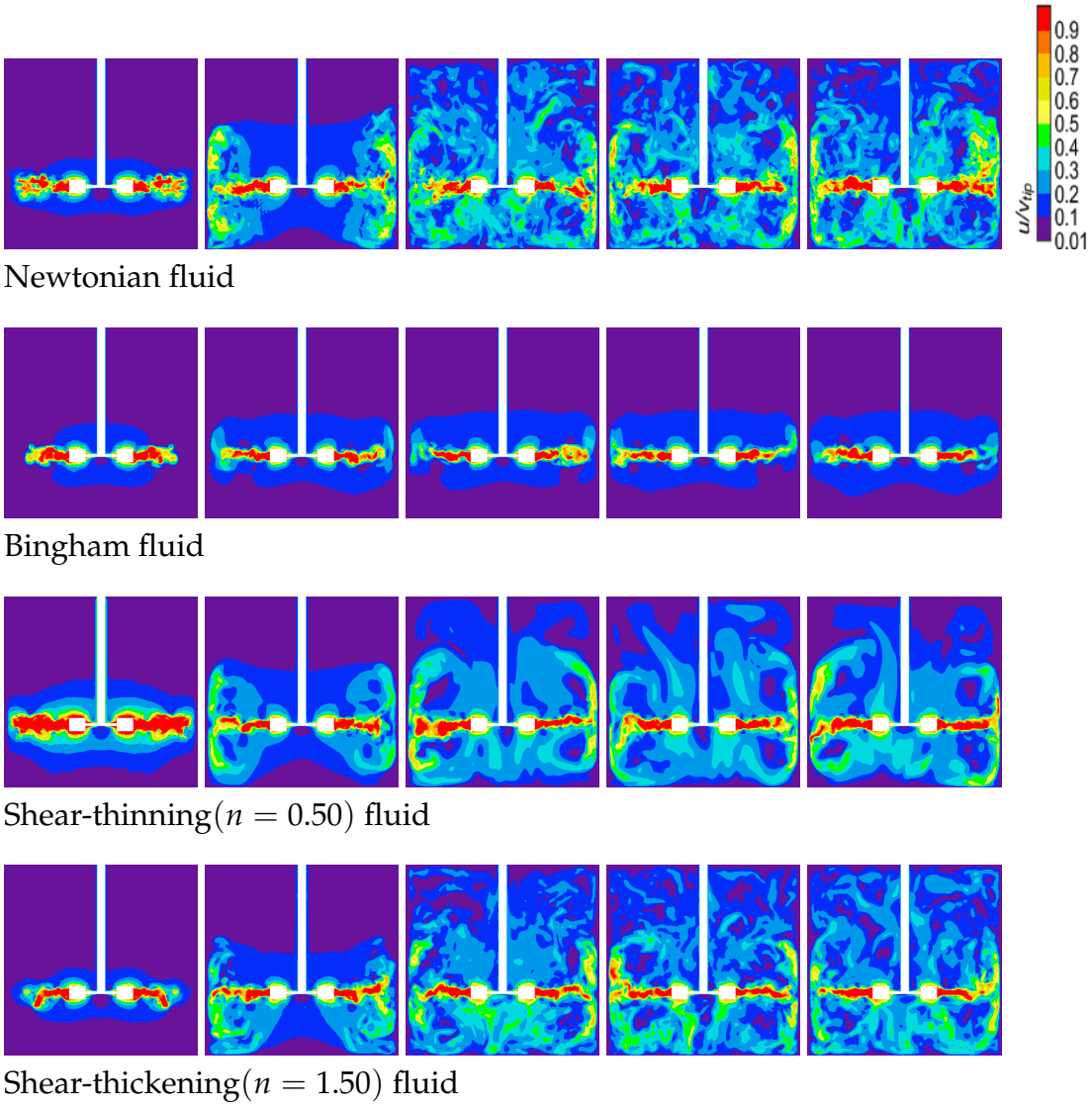

Figure 4.3: Absolute velocity $|u|/V_{tip}$ snapshots in the mid-baffle plane for the base cases (whose properties have been given in table 4.1). Left to right $tN = 1, 5, 15, 20, 30$

4.2.2 Average viscosity profiles

Before beginning the discussion on viscous effects, it is important to know how the viscosity is changing for the cases of shear-dependent-viscosity models. Fig.4.4 and 4.5 shows vertical viscosity profile radially averaged in the mid-baffle plane. Clearly we anticipate the dynamics at the impeller region to be markedly different from the other regions. As expected, the viscosities of the shear-thinning and

Bingham fluid show a decrease around the region of the impeller and are in the horizontal plane carrying the mid-half of the trailing vortex. Owing to high yield stress 12.67Pa ($Y = 0.0218$) and consequently laminar nature of its flow, the Bingham viscosities have been multiplied by factor of 100 to fit into plot. Since shear-thickening fluids become more viscous with agitation, around the same plane the fluid viscosity is highest (a factor of 3 more than viscosity at the top of the tank). At the same Re, vertical shear-thinning viscosity profiles exhibit variation with n; shown in Fig. 4.5, it can be seen that vertical profiles become blunter with increasing n, indicating weakening viscous effects as $n \rightarrow 1$. It should be emphasized that the average viscosity profiles presented are averaged in three respects i.e. with respect to time, angle, and the radius. Other averages such as those presented in the contours of turbulent kinetic energy and anisotropy are averaged with time and over angle to give a 2D plot in (r,z).

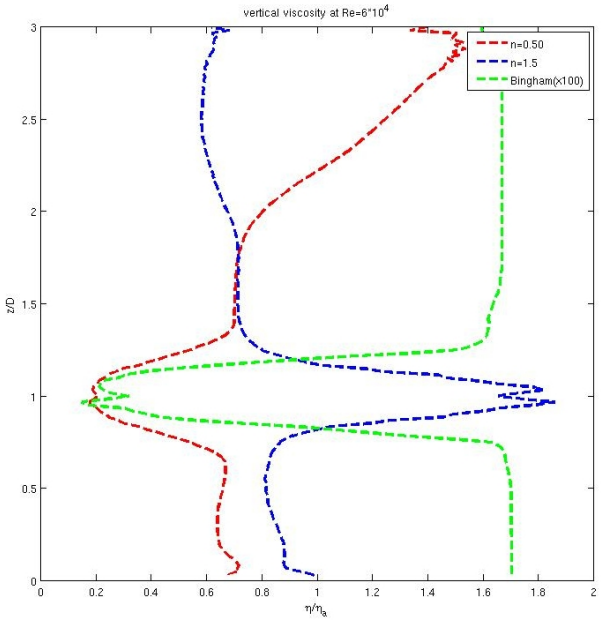

Figure 4.4: Vertical viscosity profile through mid baffle plane for the Bingham, shear-thinning and shear-thickening liquids

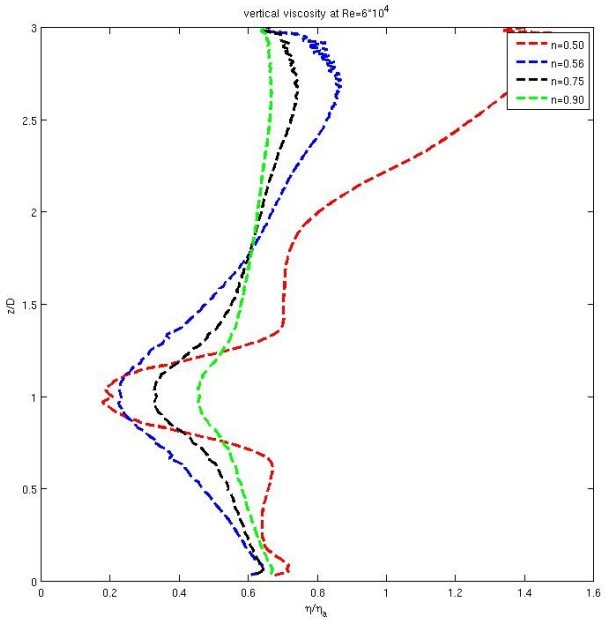

Figure 4.5: Vertical viscosity profile through mid baffle plane for the various shear-thinning liquids all at Re=6×10^3

4.2.3 Turbulent kinetic energy

In the processing of the averaged quantities i.e. turbulent kinetic energy and anisotropy, only the truly turbulent contributions of the velocity were considered. This is in view of the fact that, the blade passage contributes periodic fluctuations to the truly random turbulent motion [8]. This is the usual approach in many publications and angle-resolved averages has been employed in a number of studies [6] in which k is defined as:

$$k = \frac{1}{2}(\overline{\langle u_i^2 \rangle_\theta - \langle u_i \rangle_\theta^2})$$

with u_i indicating velocity in i-th direction, $\langle\rangle_\theta$ denotes time average value at θ, and overbar $\overline{(\,)}$ denote averaging over all angular positions. The trailing vortex core and impeller outflow regions are known to have high TKE. In addition to these regions, the circulating loops possess large amounts of TKE for the fluids without yield stress.

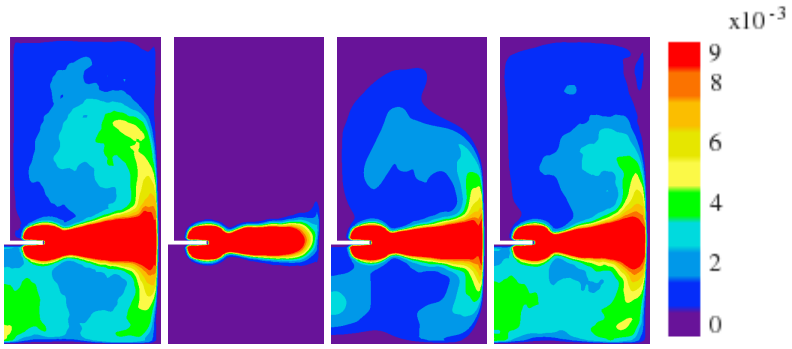

Figure 4.6: Vertical axisymmetric contours of kinetic energy k/V_{tip}^2 through mid baffle plane (from left to right) Newtonian, Bingham, shear-thinning and shear-thickening liquids in the base case simulations.

From the contours shown in Fig.4.6, it is clear that the Bingham case is laminar and its high yield stress or Bingham number is responsible for the small cavity formed. For this reason, the Bingham case will be ignored in further discussions of turbulent kinetic energy and anisotropy. In addition, the shear-thinning case exhibits a pseudo-cavity around the impeller. And regions around this pseudo-cavity have zero liquid kinetic energy typical of cavern forming likes Bingham. A flashback at the instantaneous velocity structures indicate a pseudo-cavity formation in the shear-thinning case. It is known, experimentally though, that highly shear-thinning liquids $(n < 0.3)$ usually forms a cavity during agitation [9, 10] although the mechanism for this still remains elusive. It can be shown through a parameter study that the rheological behavior (precisely, the shear stress vs. strain rate) of lower n, behave nearly like a yield stress fluid. This illustration is shown in the appendix.

Closer inspection of contours of non-yield stress fluids, especially the impeller outflow regions, the lower and upper arms of the circulating loops, it can be seen that the size of surface regions of high kinetic energy (where $k/V_{tip}^2 \geq 6 \times 10^{-3}$) is larger in the Newtonian liquid than in the shear-thickening and shear-thinning; this translates to in figures, 18.8%, 15.6% and 12.1% respectively.

4.2.4 Viscous dissipation

One possible reason for these observed differences in TKE could be viscous dissipation ϵ of turbulent kinetic energy. Because it occurs at the scales at which viscosity is important, it is reasonable to expect the varying shear-dependent-viscosities(in the power-law liquids) to have varying viscous dissipation rates all other things being equal. Viscous dissipation in this work was computed from the kinetic energy fields using $\epsilon = Ak^{3/2}/L$. In the literature L is sometimes argued to be the integral length scale [11] or based on the dimensions of the impeller [12,13]. In this work as in [12] $L = D/10$; this choice is reasonable in the impeller outflow region where we consider.

Fig.4.7 plots ϵ in the impeller outflow region normalized by N^3D^2. The profile was drawn at $r/R = 1.5$ with $z/R = \pm 0.4$ (where to $z/R = 0$ is the impeller disk height). It could be seen that the Newtonian liquid recorded the highest dissipation energy followed by the shear-thinning and then shear-thickening. The figure on right was made with the Newtonian liquid only but various values of the constant A found in the literature. Also in this figure, a comparison is made with experimental data of Wu et al [11]. The fact that the different liquids show variation in the trend of ϵ plot is still of use, although it does not directly support the initial assumption that differences in kinetic energy levels is caused by viscous dissipation.

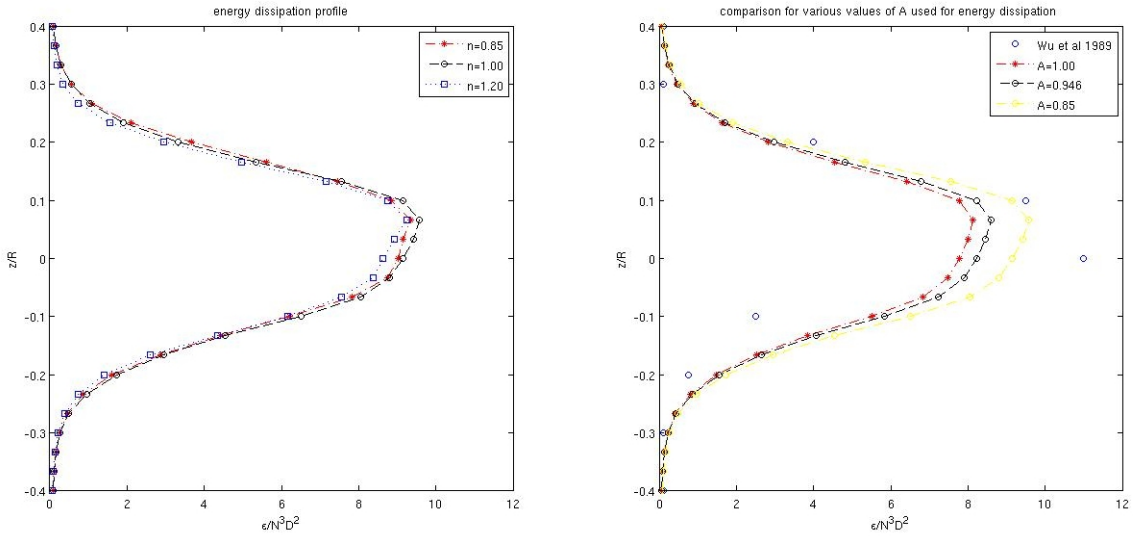

Figure 4.7: viscous dissipation ϵ/N^3D^2 in mid-baffle vertical plane at $r/R = 1.50$, plots for shear-thinning$(n = 0.68)$, shear-thickening$(n = 1.20)$ and Newtonian all at Re=1.25×10^4.

A survey of the literature explained the differences in TKE profiles between Newtonian and shear-thinning liquids on the bases of the "extra" viscous diffusion terms that appear in the transport equation of TKE [14]. When instantaneous apparent non-Newtonian viscosity $\tilde{\nu_a}$ is decomposed to the average and fluctuating apparent viscosity as in, $\nu_a + \acute{\nu_a}$ where $\overline{\acute{\nu_a}} \neq 0$, the viscous diffusion terms of the TKE equation now has two extra terms i.e.

$$\frac{\partial}{\partial x_j}\left(2\nu_a\overline{u_i s_{ij}} + 2\overline{\acute{\nu_a} u_i} S_{ij} + 2\overline{\acute{\nu_a} u_i s_{ij}}\right) \tag{4.2}$$

where $s_{ij} = \frac{1}{2}\left(\frac{\partial u_i}{\partial x_j}\right)$ and u_i is the fluctuating velocity in the i-th direction. Similar extra terms are found for ϵ in the TKE equation of the shear-dependent liquids (or technically generalized Newtonian liquids). Viscous dissipation was also found to be higher in the Newtonian liquid than in shear-thinning liquid in the data of Pinho & Whitelaw [14]. Please refer to the appendix for details on the derivation of the TKE for generalized Newtonian liquids.

4.2.5 Turbulent (an)isotropy

In characterizing the level of (an)isotropy in the tank the approach of Galletti et al [15] is considered. They define the anisotropic tensor as:

$$a_{ij} = \frac{\overline{\langle u_i u_j \rangle}}{2k} - \frac{1}{3}\delta_{ij} \tag{4.3}$$

where δ_{ij} is the Kronecker delta function. The tensor has three eigenvalues $(\lambda_1, \lambda_2, \lambda_3)$ whose its invariants are given by:

$I = \lambda_1 + \lambda_2 + \lambda_3 = 0; \quad II = \lambda_1\lambda_2 + \lambda_2\lambda_3 + \lambda_1\lambda_3; \quad III = \lambda_1\lambda_2\lambda_3$. And finally, defining a parameter $|A|$, where $|A| = \sqrt{III^2 + (-II)^2}$ is the distance from isotropy. Thus, a value of $|A|$=0 indicates an absolute isotropic state and 0.09 indicates high anisotropy. It must be said that this approach yields a maximum possible value of 0.103 which corresponds to 0.42 in the data of Derksen et al [16]. Contours of $|A|$ are shown in Fig.4.8a-c; the figures shown are taken from the mid-baffle plane which does not section through the impeller blades unlike the figures in [15] who also presented vertical contours of the distance from anisotropy. Nonetheless, we get a picture of the areas where both cited references have high turbulent anisotropy, which are at the impeller outflow and bottom of the tank [15, 16] and regions around the centers of the circulation loops [15].

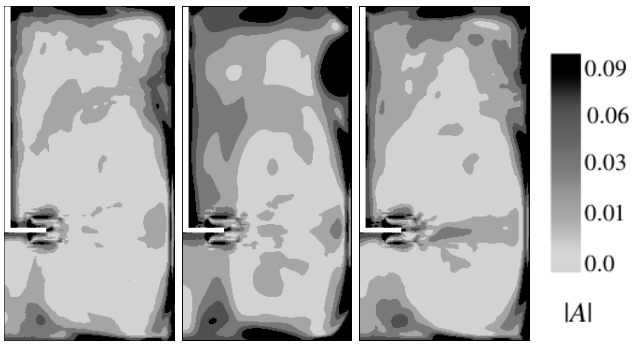

Figure 4.8: Contours of $|A|$ (distance from anisotropy) from left to right: Newtonian, shear-thinning and shear-thickening liquid for the base case simulations.

4.2.6 Shear-thinning mean velocity profiles

Recently, Venneker et al [17] have demonstrated that shear-thinning liquids in stirred tanks exhibit some variation with Re and n at the disk height and tip of impeller blade. In view of that, a second string of simulations were started for only shear-thinning fluids at Re$= 6 \times 10^3$, and $n = 0.56, 0.75$ and 0.90. The mean disk height(MDH) velocity profiles are read at impeller disk height $z/T = 1/3$ for all three velocity components i.e. axial, radial and tangential. The empirical correlations for these profiles are:

$$\frac{W}{V_{tip}} = \frac{1}{\frac{1}{0.676} + 8.48ln(\frac{r}{R})} \tag{4.4}$$

This gives the mean disk height tangential velocity; the radial V, and axial U, are as follows:

$$\frac{V}{V_{tip}} = 0.785 \left(\frac{r}{R}\right)^{-1.11} tanh\left(3.63\left(\frac{T}{D} - \frac{r}{R}\right)\right) \tag{4.5}$$

$$\frac{U}{V_{tip}} = -0.109 + 0.228 \left(\frac{r}{R}\right)^{-0.704} tanh^2\left(2.34\left(\frac{T}{D} - \frac{r}{R}\right)\right) \tag{4.6}$$

It must be emphasized that these equations are "purely descriptive" and were generated by commercial software TableCurve2D (refer to [17] for details).

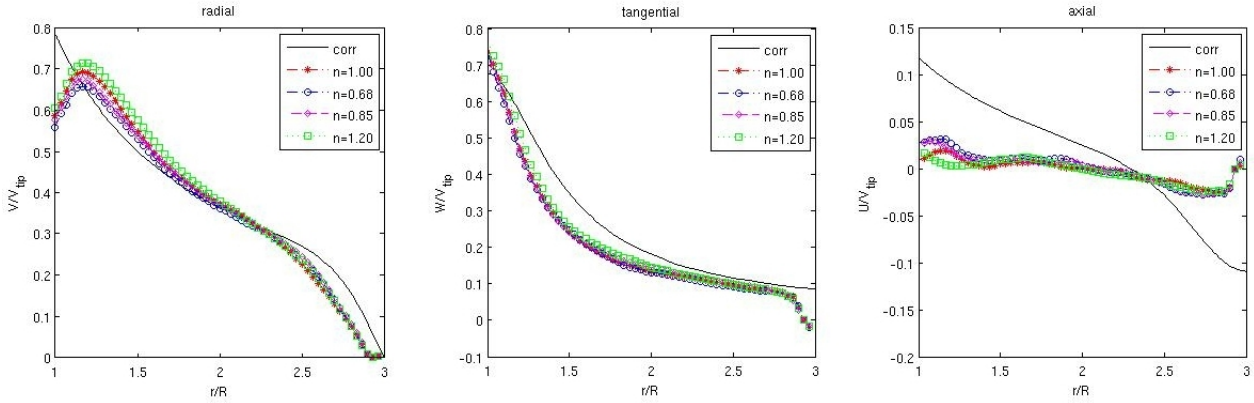

Figure 4.9: Mean disk height velocity profiles for different n (left to right) radial, tangential and axial velocity profiles.

From Fig. 4.9a-b it can be seen that the radial and tangential correlations provides acceptable fit to MDH profiles; the correlation for the axial profile (Fig. 4.9c) does rather poorly as it neither falls within boundaries nor capture trend. The dependency on n for the radial and tangential profiles at $1.0 \leq r/R \leq 1.3$ can be said to be slight.

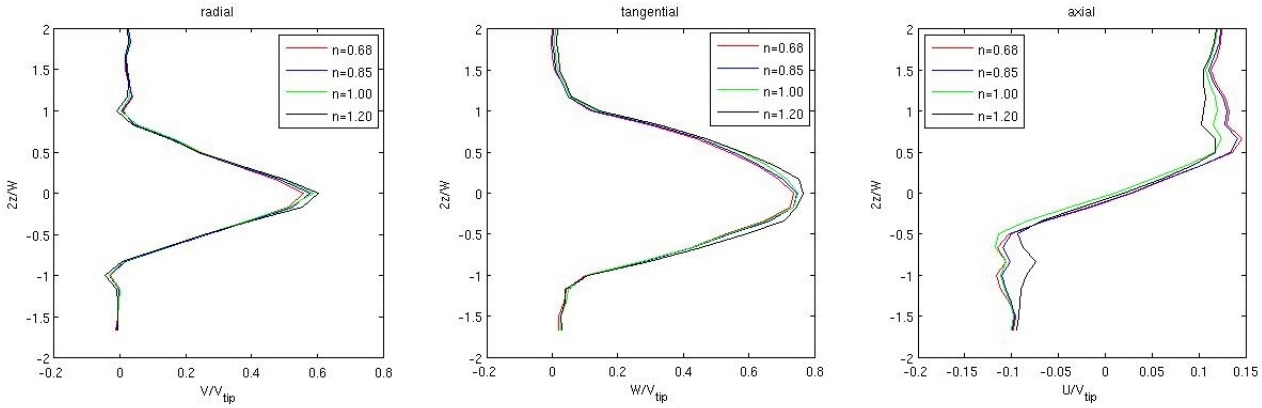

Figure 4.10: Mean discharge velocity profiles for different n (left to right) radial, tangential and axial velocity profiles.

Discharge velocity profiles defined as "velocity profile along the blade at its tip" in Fig. 4.10a-c show the profile widening effect with n as Venneker et al [17] observed. In this case too the axial discharge profile exhibited invariance to n. There is also a weak dependency on n when one examines the three fluctuating rms velocity profiles presented in Fig. 4.11a-c. Profiles indicate in addition to the tangential rms velocity which is known to exhibit a dependency on n, the axial rms also shows this dependency. The radial rms velocity however, shows no sensitivity to n.

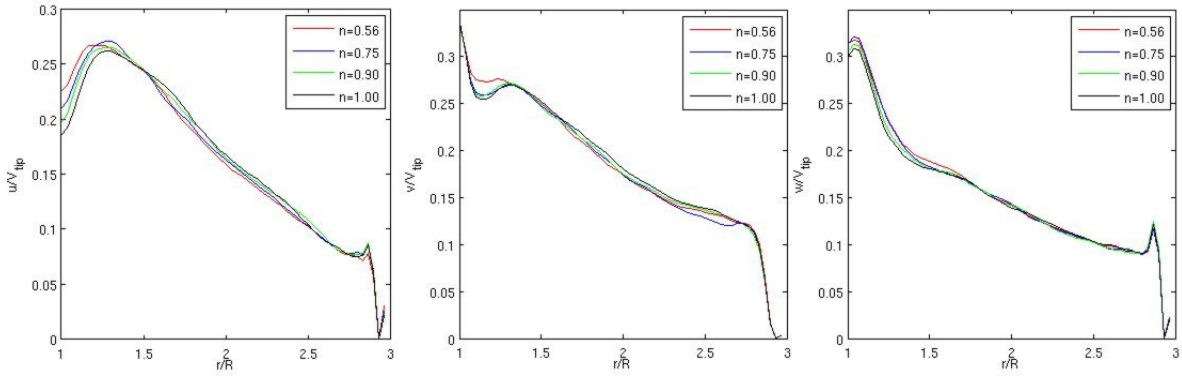

Figure 4.11: Fluctuating rms velocity profiles for different n (left to right) axial, radial, and tangential velocity profiles.

4.2.7 Non-Newtonian Power Number

The power number is one important and widely used dimensionless group for agitator design specification [18]. Engineers have long since worked with correlations from experimental results for Newtonian power numbers with 6-blade turbine ever since Rushton et al pioneered this work in the 1950's. More recent investigations include Hockey [19] and Distelhoff [20]. Work on non-Newtonian fluids dates back in the late 1950's [1] and although a lot correlations and experimental results exist, there are hardly any that go beyond Re$= 10^3$. Hockey [19] identified a difficulty in prescribing a truly representative viscosity to define a working Reynolds number. Nevertheless he applied Metzner and Otto's average shear rate approach and recorded experimental data for shear-thinning and Newtonian fluids over a wide range of Reynolds numbers ($10^2 - 10^5$). The power numbers in this work are determined from the torque and shaft speed $N_P = \frac{T_q \Omega}{\rho N^3 D^5}$, where the torque is the cross product of the radial arm vector and the force vector, given as: $T_q = \mathbf{r} \times \mathbf{f}$. Our simulation of Newtonian and shear-thinning $(n = 0.5)$ liquids at Re$= 6 \times 10^3$ gives a power number of 3.63 and 3.47 respectively. Hockey's experimental data indicate 3.9 ± 0.1 and 3.8 ± 0.1 for the Newtonian and shear-thinning liquids respectively. Although it must be said that flow indices in his work are much different from that of this work.

4.3 Conclusion and outlook

The response of non-Newtonian fluid behavior to turbulent stirred tank conditions has been explored using Bingham, shear-thinning and shear-thickening liquids. Except the Bingham case which happened to be laminar, flow structures are similar to the Newtonian case.

- The shear-thinning liquid formed a pseudo-cavern observed for this rheology but at lower flow index. Among the non-Newtonian liquids the shear-thickening exhibited greatest turbulence in terms of velocity magnitude distribution TKE.

- Simulations indicate that TKE is higher in Newtonian liquids than in non-Newtonian liquids; the same trend is observed in the Reynolds stresses. Among the non-Newtonian liquids, shear-thickening liquid exhibited higher turbulent conditions in terms of TKE than shear-thinning.

- Also, energy dissipation, as seen in a radial profile at $r/R = 1.5$ in the impeller outflow region, is higher in Newtonian liquid than in shear-thinning and followed by shear-thickening. The differences in TKE were traced to the extra terms that appear in the viscous diffusion term in the TKE equation of shear-dependent liquids. The same line of reasoning is applied to the viscous dissipation trend (which also has 2 extra terms due to fluctuating viscosity) observed in these liquids.

- Turbulent anisotropy was characterized by distance from isotropy $|A|$ – a technique that has been employed in a number of studies. The distribution of turbulent anisotropy agrees very much to what is reported in the literature, i.e. in the plane of the trailing vortex, the bottom of the tank, and in the centers of the circulating loops.

- Since simulations with the lattice-Boltzmann method give highly resolved flow data, our simulations compare very well to the empirical correlations

in [17]. Results from our simulations indicate the radial and tangential MDH profiles exhibit a slight dependency on n. The widening effect of profile with n observed experimentally is also seen in our simulation for the radial and tangential profiles. Then, in addition to the tangential, axial rms velocity profile also shows a weak dependency on n.

- The power number for shear-thinning liquids of different n but at the same Re, gives reasonable agreement with experimental data found in the literature.

In this chapter, the simple power-law equation was used to characterized the viscous behavior of the shear-dependent viscosity liquids. One drawback of this equation is its instability in very low- and high- shear regions. Although this issue was not observed in this work, it will be useful to check with other models. If one desires a more accurate representation of the viscosities in these liquids then higher parameter models like the Carreau or Ellis models can be used. Of course these models come with their challenges, as in the application of these models one has to find a natural way of handling and representing the extra parameters in these models.

Bibliography

[1] Metzner, A.B., Otto, R.E., "Agitation of non-Newtonian liquids" AICHE Journal 3, 3, 1957

[2] Wu, J., Graham, J., Mehidi, N.N., "Estimation of Agitator Flow Shear Rate" AICHE Journal , 52, 7, 2006

[3] Ostwald, W., Kolloid-Zeitschrift, 36,99-117, 1925; Waele, A. de., Oil Color Chem. Assoc. J., 6, 33-88, 1923

[4] Beverly, C.R.; Tanner, R.I. Numerical analysis of extrudate swell in viscoelastic materials withyield stress. J. Rheology, 33, 989,1989

[5] Derksen, J.J., "Solid Particle Mobility in agitated Bingham liquids" , Industrial & Engineering Chemistry Research, vol. 48, p2266, 2009

[6] Derksen, J. J., Van den Akker,H. E. A., ''Large Eddy Simulations on the Flow Driven by a Rushton Turbine,'' AIChE J., 45(2)209., 1999

[7] Goldstein, D., Handler, R., Sirovich, L., "Modeling a No-Slip Flow Boundary with External Force Field ", J. Comput., Phys., 105, 354, 1993

[8] Van't Riet, K., "Turbine Agitator Hydrodynamics and Dispersion Performance", PhD thesis, TU Delft, 1975

[9] Elson, T. P., Cheesman, D. J., Nienow, A. W., "X-ray studies of cavern sizes and mixing performance with fluids possessing a yield stress", Chem. Eng. Sci., 41, 2555–2562,1986

[10] Paul, E. L., Atiemo-Obeng, V.A., Kresta, S.M., "Handbook of Industrial Mixing", John Wiley & Sons, Inc., ISBN: 0-471-26919-0, 2004

[11] Wu, H., Patterson, G.K., Doorn, M. V., "Distribution of Turbulence Energy Dissipation Rates in a Rushton Turbine Stirred Tank" Expt. Fluids 8, 153160, 1989

[12] Venneker, B.C.H., "Turbulent Flow with Gas Dispersion in Stirred Vessel with Pseudoplastic liquids" PhD Thesis, TU Delft, 1999

[13] Kresta, S.M., Wood, P., "The Flow Field Produced by a Pitched Blade Turbine: Characterization of the Turbulence and Estimation of Dissipation Rate", Chem. Eng. Sci., 48, 1761-1774, 1993

[14] Pinho, F.T., Whitelaw, J.H., "Flow of non-Newtonian Fluids over a Confined Baffle", J. Fluid Mech., 226, p475-496,1991

[15] Galletti, C., Brunazzi, E., Pintus, S., Paglianti, A., Yianneskis, M., "A Study of Reynolds Stresses, triple products and turbulent states in a radially stirred tank with 3D Laser Anemometry" Chemical Eng. Res. Design, 82(A), 1214-1228, 2004

[16] Derksen, J. J., Doelman, S., Van den Akker,H. E. A., "Three-dimensional LDA Measurements in the Impeller Region of a Turbulently Stirred Tank" Experiments in Fluid 27, 522-532, 1999

[17] Venneker, B.C.H., Derksen, J.J., Van den Akker, H., "Turbulent non-Newtonian Flow in a Stirred Tank-LDA Experiments on the influence of Reynolds Number and Flow Index", Chemical Engineering Research and Design, Preprint, 2008

[18] Chapple,D., Kresta, S.M., Wall, A., Afacan, A., "The Effect of Impeller and Tank Geometry on Power Number for a Pitched Blade Turbine ", Trans IChemE, vol 80, Part A, 2000

[19] Hockey, R. M., "Turbulent Newtonian and non-Newtonian flows in stirred vessels" PhD thesis, Imperial College of Science, Tech. & Medicine, 1990

[20] Distelhoff, M.F.W., Laker, J, Marquis, A. J., Nouri, J.M., "Application of Strain Gauge Technique to the Measurement of Power Characteristics of five Impellers", Experiments in Fluids, 20 56-58,1995

5 Solid particle motion in turbulently agitated non-Newtonian liquids

The response of non-Newtonian behavior to turbulent stirred tank conditions was explored in the previous chapter. Turbulent characteristics such as turbulent kinetic energy and anisotropic states were observed to have subtle differences although velocity flow structures and circulation patterns in the tank were structurally similar.

The purpose of this work is to examine and possibly identify the effect of non-Newtonian rheology on the turbulence characteristics as well as the settling and distribution of solids in a stirred tank. There is not much to find in the literature concerning solid particles in turbulently agitated non-Newtonian carrier liquids. It is understood that the complexity of turbulence and the variety of non-Newtonian characteristics [1, 2] is the reason for limited research into turbulent flow of non-Newtonian liquids. The Lattice-Boltzmann method, LBM, is employed in the direct numerical simulation of liquid-phase while discrete particle modeling is used in the modeling of the solid-phase in this two-phase flow. In all simulations, the suspensions are dilute -3.29% by mass fraction and so simulations are one-way coupled (i.e. particles "feel" the liquid but doesn't influence liquid). This assumption has been investigated and proven reasonable by Picciotto et al [3] who studied modulation by particles over solid boundary layers.

The outline of this chapter is as follow: first, a section on description of the flow

systems and cases in terms of flow geometry, liquid characteristics and simulation procedure; this is followed by presentation of particle dynamics where the various forces acting on particles in the tank are presented and method of implementation is also discussed. Then after, a results and discussions on particle velocity fields, vertical solids distribution, effect of Reynolds number, impact of Stokes number section is next; and the chapter is then tailed by a conclusion.

5.1 Flow system and cases

The stirred tank simulated is a standard 10L lab-scale tank equipped with four baffles with a Rushton turbine mounted at clearance T/3 from bottom. Fig. 5.1 gives details of its configuration and dimensions. Observe that $D = T/3 = 7.78 \times 10^{-2} m$; and the top of the tank is closed like the tank used in Chapter 4 as this prevents air entrainment.

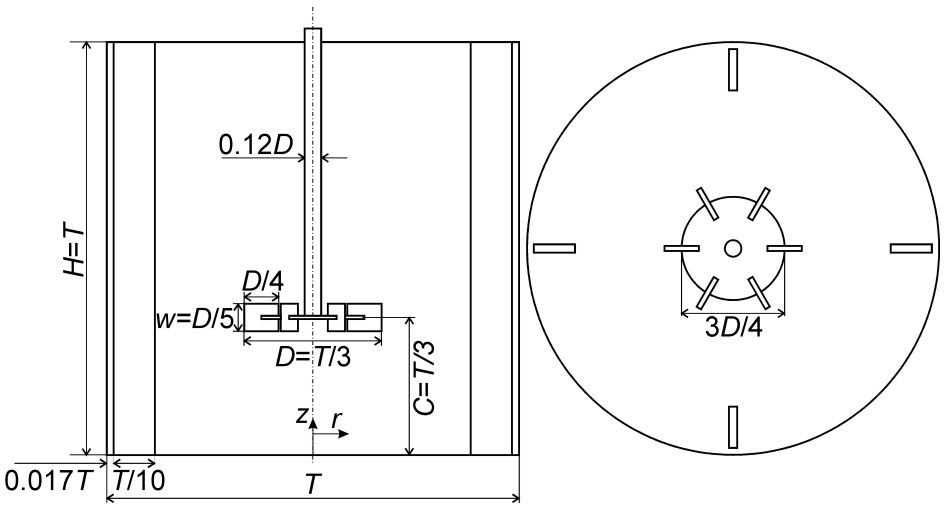

Figure 5.1: Tank geometry; midway view of the tank (left), vertical cross-section view at z=T/3 and dimensions of impeller blades in (r,z) co-ordinates. Source: Derksen [4]

In the base case simulations, for each Re, $6.0 \times 10^3, 8.5 \times 10^3, 1.25 \times 10^4$ four simulations were set-up with flow indices n = 0.68, 0.85 1.00 (Newtonian) and 1.20. The Herschel-Bulkley cases were done at Re = 8.5×10^3 and n =0.68, 0.85 and 1.20; also, the Yield-stress number (refer to previous section for definition) for these

simulations was always Y =1.83 $\times 10^{-3}$. The choice of Re and n are inspired by data available in the literature, hence are known a priori like D and liquid density $\rho_l = 10^3 \text{Kg}/m^3$. The formal presentation of the cases simulated is shown in table 5.1 below. The definition of Re, is based on Metzner & Otto [5] concept of "average" shear in the derivation of the mean apparent kinematic viscosity. Please refer to section 4.2 of the previous chapter on apparent viscosity determination for the power-law liquids. For the case of the Herschel-Bulkley fluid model, the apparent viscosity is given as Eqn 3.20. We define Reynolds number as previously Eqn 4.1 but repeated here for convenience.

$$Re = \frac{\rho_l N D^2}{\eta_a} \tag{5.1}$$

N is chosen to be 30rev/s and thus, the only unknown in (5.1) can now be found and further used in finding the consistency index, K of the power-law and Herschel-Bulkley fluid. Note that the exact definition of η_a depends on the rheology of the fluid as $\eta_a = \mu$ for Newtonian, $\eta_a = K\dot{\gamma}_a^{n-1} = K(\pi N)^{n-1}$ for the power-law liquids and $\eta_a = \tau_0/\dot{\gamma} + K\dot{\gamma}^{n-1}$ for the Herschel-Bulkley fluids. In the simulations particles are mimicked as rigid spheres initially uniformly randomly distributed throughout the tank. All particles used had diameter of $0.65mm$. Except for case 3B which had density ratio $\rho_s/\rho_l = 1.70$ all other cases had $\rho_s/\rho_l = 2.50$; also mass fraction of solids was 3.29% for base case simulations. The Stokes number $Stk = \left(\frac{\rho_p N d_p^2}{18\eta_a}\right)$, defined as, ratio of Stokesian particle relaxation time and the time of one impeller revolution was set to less than unity to ensure particle flow closely couples to that of the liquid flow field as simulations are one-way coupled. The choice of impeller speed $N = 30$rev/s is judicious given the fact that it exceeds the Zwietering [6] just suspended criterion given as:

$$N_{js} = s\frac{d_p^{0.2}\eta_a^{0.1}(|g|\Delta\rho)^{0.45}\Phi_m^{0.13}}{\rho_l^{0.55}D^{0.85}} \tag{5.2}$$

this gives N_{js} values of 22.7, 21.9 and 21.6 rev/s for Re=$6.0 \times 10^3, 8.5 \times 10^3, 1.25 \times$

10^4 respectively. The application of N_{js} to non-Newtonian suspensions seems expedient in the view of the author given the absence of correlations for particle settling in non-Newtonian liquids.

cases(#)	$\mathrm{Re}\times10^3[-]$	n [-]	$\eta_a \times 10^{-2}[Kg/m/s]$	$Stk \times 10^{-2}[-]$	$Y\times10^{-3}$
1A(4)	6.0	0.68,0.85,1.00,1.20	3.04	5.78	-
2A(4)	8.5	0.68,0.85,1.00,1.20	2.15	8.24	-
2B(3)	8.5	0.68,0.85,1.20	2.15	8.24	1.83
3A(3)	12.5	0.85,1.00,1.20	1.46	12.1	-
3B(2)	12.5	0.85,1.00	1.46	8.24	-

Table 5.1: Fluid characteristics and *Stk* of the various cases in this work

As indicated earlier, LBM is employed in the solution of the equations of motion of the fluid. The 10L tank is simulated on a cubic grid of size 180^3. Boundary conditions on the static (cylindrical tank wall and baffles) and non-static (impeller) were imposed by an immersed boundary technique also known as the adaptive force technique [7]. The spatial resolution was such that the tank diameter T corresponded to 180 grid spacings, $\Delta = T/180 = 1.3mm$. The impeller makes a complete revolution in 2000 time steps, thus, 1 time step (also temporal resolution) of the simulation is $(2000N)^{-1}$ = $16.67\mu S$ on the wall clock.

5.2 Particle dynamics

Modeling of particle dynamics was done following the approach of Derksen [4]. A particle at position $\mathbf{x}_p$ has three degrees of freedom i.e. three linear co-ordinates (no rotational co-ordinates because particle rotation has been neglected in these simulations). And its equations of motions are solved by:

$$\frac{d\mathbf{x}_p}{dt} = \mathbf{v}_p \qquad \rho_s \frac{\pi}{6} d_p^3 \frac{d\mathbf{v}_p}{dt} = \sum \mathbf{F} \tag{5.3}$$

with $\mathbf{v}_p$ the velocity of the particle and forces in consideration being net gravity $\mathbf{F}_g = (\rho_s - \rho_l)\frac{\pi}{6} d_p^3 \mathbf{g}$ where $\mathbf{g}$ denotes force of gravity; the drag force is given by: $\mathbf{F}_D = C_D \frac{\pi}{4} d_p^2 \frac{1}{2} \rho_l |\mathbf{u} - \mathbf{v}_p|(\mathbf{u} - \mathbf{v}_p)$ (C_D and $\mathbf{u}$ denote drag coefficient acting on parti-

cle and liquid velocity respectively). Added mass force given by $\mathbf{F}_{AM} = \frac{1}{2}\rho_l \frac{\pi}{6} d_p^3 \frac{d\mathbf{v}_p}{dt}$ is considered in this work. Given the viscous nature of fluids in consideration, the drag force is expected to be the dominant hydrodynamic force; consequently, lift, stress-gradient and history forces have been neglected. The drag coefficient used is based on the Re_p as in Schiller & Naumann [8] defined as $Re_p = \frac{\rho_l |\mathbf{u} - \mathbf{v}_p| d_p}{\eta_a}$ and

$$C_D = \begin{cases} 24 Re_p^{-1}(1 + 0.15 Re_p^{0.687}) & Re_p < 1000 \\ 0.44 & Re_p \geq 1000 \end{cases}$$

In the simulation, particles collide with other particles (particle-particle collision), with the wall (particle-wall) and with the impeller blades, shaft and disk (particle-impeller). All collisions are perfectly elastic and frictionless. The collision algorithm described by Derksen [9] is applied here. A particle can collide only once in a time step. Clearly, this assumption limits the time step or number of particles in the tank at each time step, however, this method reduces the huge computational expense required to simulate multi-collisions of particles at unit time steps given the fact particle-particle collision is an M^2 where M is the number of particles; thus, for 2 collisions per particle per time step the process becomes M^3. In the event the collision detection algorithm misses a collision as in the situation where two particles are so close their mutual distance will be less than d_p in the subsequent time step, the missed collision algorithm is executed (please refer to the cited article for more on the handling of missed collision). As indicated earlier, simulations are one-way coupled; this choice is largely due to findings in a similar numerical study [4] in which two-way coupled simulations of solid particles agitated in Bingham liquids did not vary significantly from one-way coupled simulations at solids loading of 3.37%.

5.3 Results and Discussion

All simulations were initialized to a zero liquid and particle velocity flow field at start. In total, 35 impeller revolutions were simulated. Snapshots of solid particle velocities are shown in Fig.5.2–5.5. The onset of turbulence, evident in chaotic

eddy structures can be seen from $tN = 1$ and after. As we expect, the instantaneous view should provide no differences in turbulence structures of the power-law and Newtonian suspensions given the fact that these systems are structurally and dynamically similar. Among the suspensions with yield stress liquids (Herschel-Bulkley fluids), the formation of an active cavity is observed in the simulation with flow index n =0.85 and 0.68 (not shown) but not in n =1.20. This can be rationalized on the viscous behavior of the fluid. Compared to the "regular" Herschel-Bulkley fluid with $n < 1$, the fluid shear thins after the yield stress is exceeded and thus, in its velocity flow field, there will be a cavity around the impeller which of course has a size dependent on many factors including the magnitude of the yield stress, impeller clearance, etc; and around this cavity will be dead zones – areas of poor mixing where fluid is unyielded. In the dead zones, particles are held in suspension primarily by the fluid yield stress. In the case of n =1.20, the fluid shear thickens around the impeller where shear forces are greatest. This thickened fluid with higher viscosity is easily displaced surrounding less dense fluid by turbulent convection.

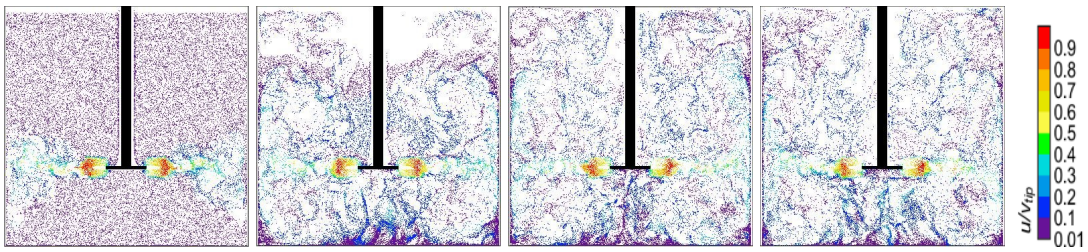

Figure 5.2: Case 3B, suspension with Newtonian liquid. Absolute particle velocity in vertical mid-baffle slice of thickness $0.01T$ at $tN = 1, 10, 15, 30$

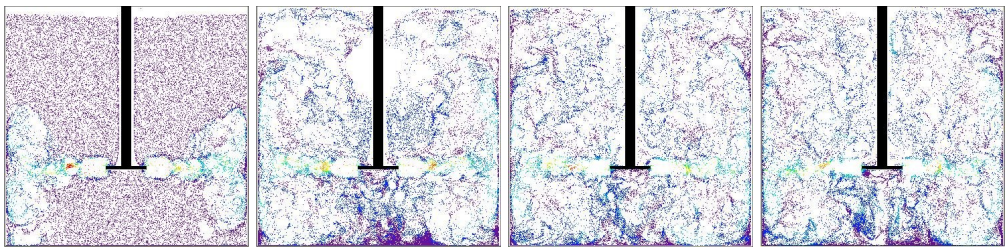

Figure 5.3: Case 3B, suspension with shear-thinning liquid. Absolute particle velocity in vertical mid-baffle slice of thickness $0.01T$ at $tN = 1, 10, 15, 30$

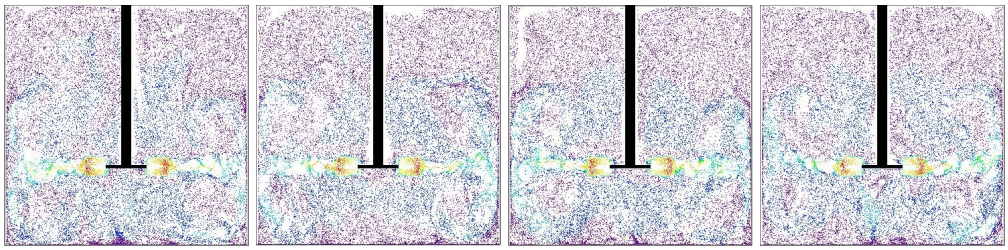

Figure 5.4: Case 2B, suspension with Herschel-Bulkley fluid $n = 0.68$. Absolute particle velocity in vertical mid-baffle slice of thickness $0.01T$ at $tN = 15, 20, 30, 35$.

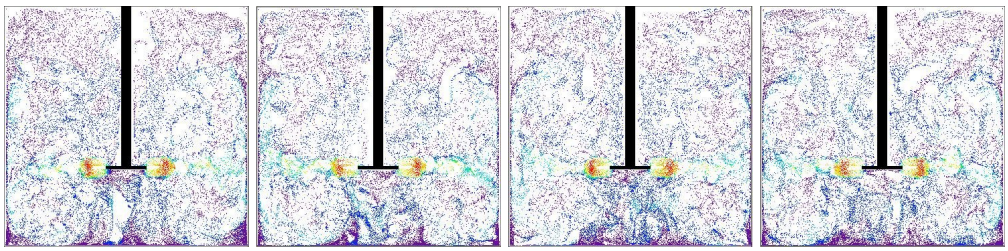

Figure 5.5: Case 2B, suspension with Herschel-Bulkley fluid $n = 1.20$. Absolute particle velocity in vertical mid-baffle slice of thickness $0.01T$ at $tN = 15, 20, 30, 35$

The viscous behavior of the shear-thickening Herschel-Bulkley fluid also affect the kinetic energy of the liquid phase. The absence of a cavity in such fluid distinguishes its liquid phase k contour from other yield stress fluids by absence of dead-zones above the cavity. Fig. 5.6 shows k contour plots of five suspensions all at Re=8.5×10^3.

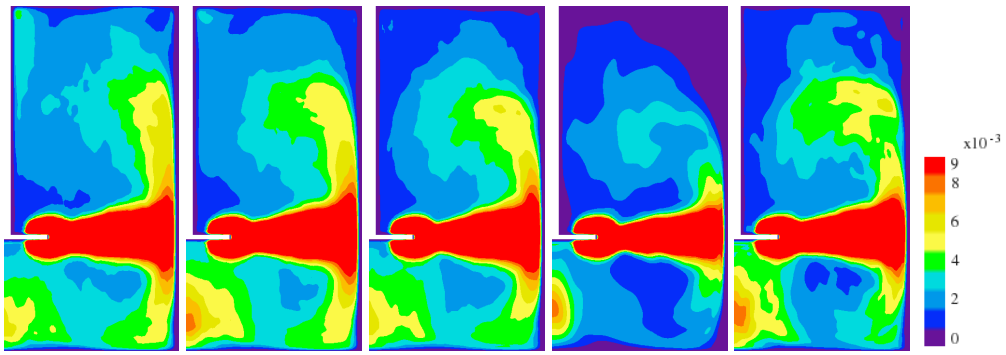

Figure 5.6: contours of k/V_{tip}^2 for shear-thinning ($n = 0.68$), Newtonian, shear-thickening($n = 1.20$), HB($n = 0.60$) and HB $n = 1.20$.

In studying how high Reynolds number affects particle settling and distribution in the tank, the author wishes to make clear once again that, for cases tested in 1A, 2A and 3A, the difference or increase in Reynolds number is a result of decreasing apparent viscosity of the working fluids. All cases were simulated with impeller speed of $N = 30rev/s$ and in the same tank settings with constant fluid density. Obviously, the increasing concentration at the bottom with Re, is as a result of reducing viscous resistance and thus, gravity pulling particles towards tank bottom much easily. Fig. 5.7 shows the effect of changing Re with n on the vertical solids concentrations. Also, particle accumulation at the tank bottom of non-Newtonian shear-thinning liquids is considerably higher than that of Newtonian liquids; and shear-thickening liquids held less particles at the tank bottom than Newtonian liquids. This too is a viscous effect, given the fact that relative viscosities (discussed in previous section in fig. 4.3) of power-law liquids at tank bottom get lower than Newtonian; and that shear-thinning being least.

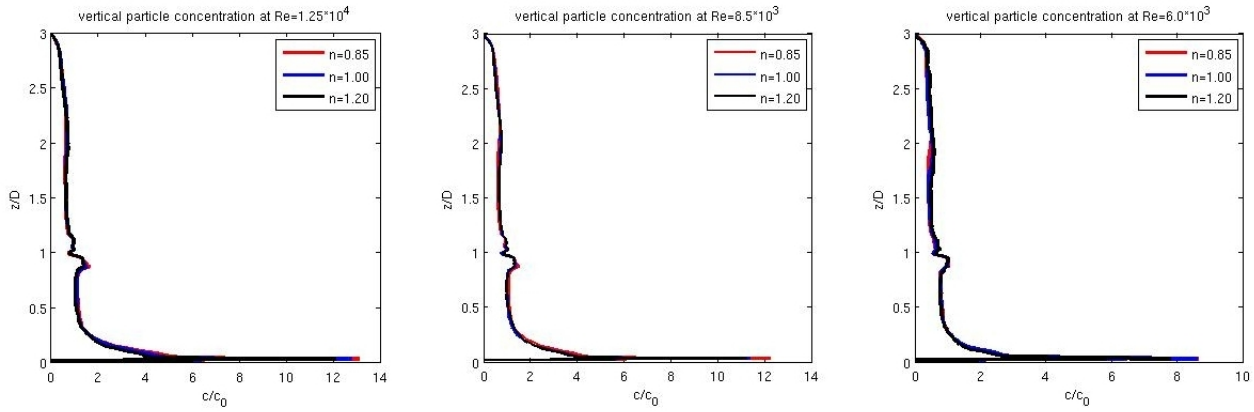

Figure 5.7: Vertical solids concentration horizontally averaged in mid-baffle plane for the different power-law liquids from (left to right) Re=1.25 $\times$ 10^4, 8.5 $\times$ 10^3 to 6.0 $\times$ 10^3.

As expected, suspensions with yield stress liquids recorded lower bottom concentration of particles than suspensions with power-law or Newtonian liquids. In similar numerical study with Bingham liquid [4], explained that the fluid yield stress keeps the particles distributed throughout the suspension. The vertical profiles in fig. 5.8 show a more uniform profile (5.8a) for the yield stress fluids in addition to the lower particle concentration at the tank bottom.

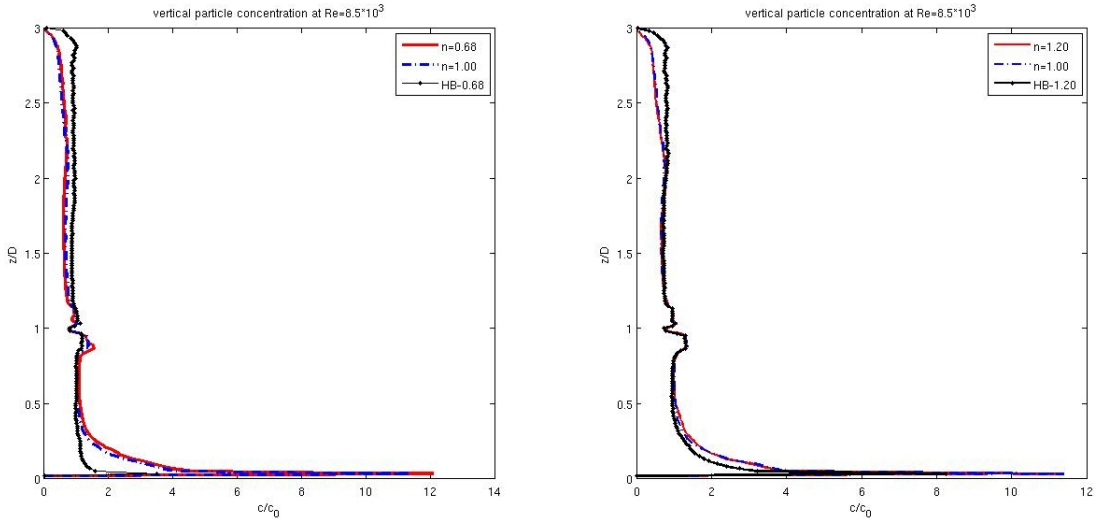

Figure 5.8: Vertical solids concentration horizontally averaged in mid-baffle plane for the (5.8a) shear-thinning and HB suspensions at n=0.68 and Re=8.5 $\times$ 10^3; (5.8b) shear-thickening and HB suspensions at n=1.20 and Re=8.5 $\times$ 10^3.

In view of the fact that initial three cases – 1A, 2A, 3A, simulated had different Stokes numbers, case 3B was implemented to investigate the impact of particle Stokes number on the solids settling. This was done by using carrier phases with higher density and this reduced the density ratio of solid to liquid, from 2.5 to 1.7. This implementation also served the additional purpose of providing insight on buoyant effects on the solid particles. In Fig. 5.9, the effect of particle Stokes number is shown to be independent of the rheology as shear-thinning and Newtonian carrier fluids both indicate that for particle settling at the bottom increases (by nearly 25%) when Stokes number increase (in this case for nearly 50% increase).

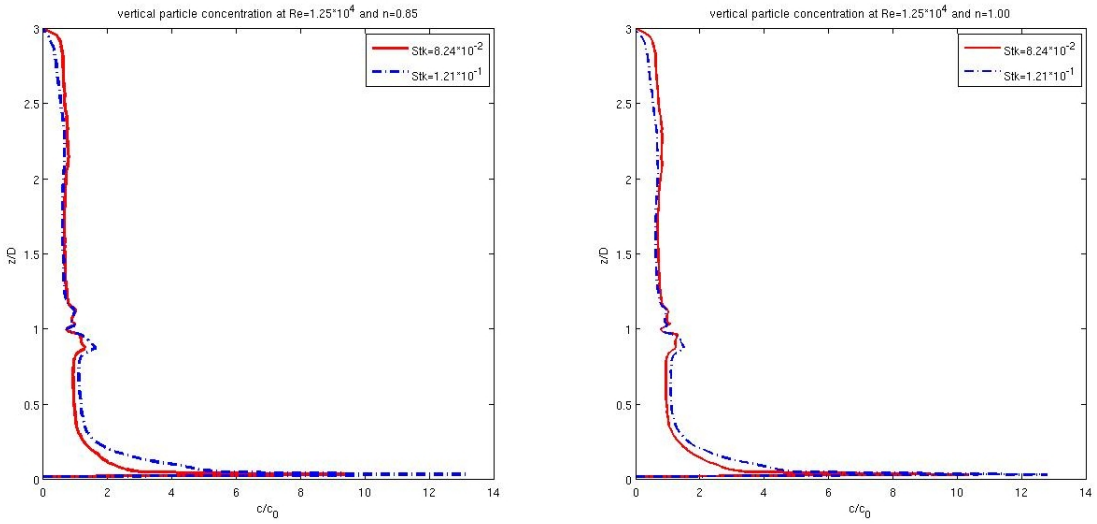

Figure 5.9: Vertical solids concentration: effect of Stk number (5.9a) shear-thinning and HB suspensions at $n = 0.85$ and Re=1.25×10^4; (5.9b) shear-thickening and HB suspensions at $n = 1.20$ and Re=1.25×10^4.

This is not unexpected, in view of the fact that reducing the density ratio between solid and liquid will inevitably increase the buoyant force acting on a particle thereby reducing net gravity force on the particle and thus minimizing drift of particles towards bottom of tank. Although, this result was expected, it invariably clarifies doubts about the dominant forces which was acting on the particles in tank; which was initially not clear given the presence of viscous effects in the non-Newtonian liquids. Initially, it was reasoned that at the high solids concentration at the bottom of non-Newtonian suspensions was caused by non-Newtonian ef-

fects acting to increase local viscosity as well as thickening of the viscous sublayer to trap particles into that region. At the same Stk, when Re is increased particles show increasing tendency towards the bottom shown in Fig. 5.10

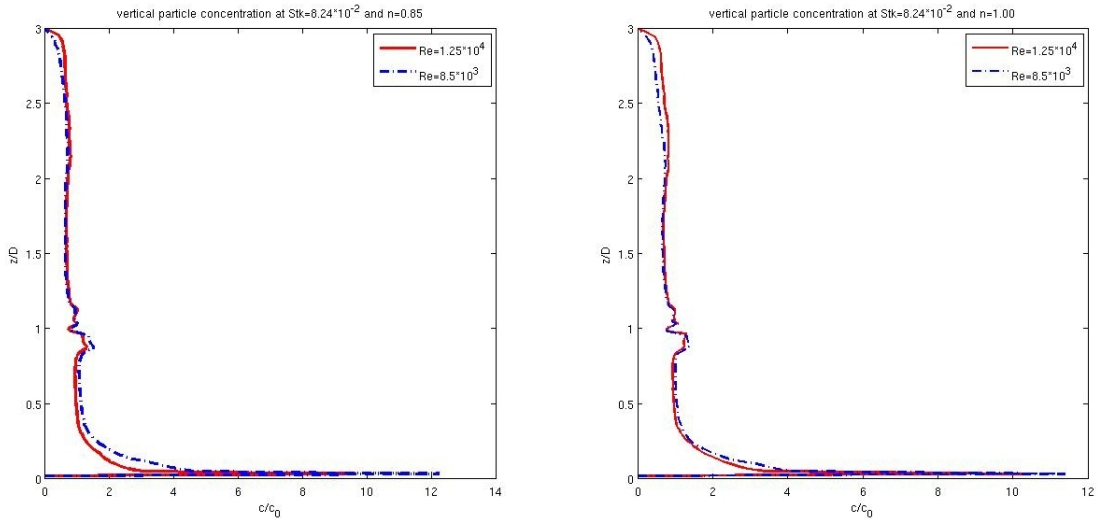

Figure 5.10: Vertical solids concentration: effect of Re on Stk number (5.10a) shear-thinning and HB suspensions at $n = 0.85$ and $Stk = 8.24 \times 10^{-2}$; (5.10b) shear-thickening and HB suspensions at $n = 1.20$ and Stk8.24×10^{-2}.

In a side study, the solids mass fraction was increased (to 6.63%) in two simulations of shear-thinning $n = 0.68$ and Newtonian all at Re=8.5×10^3. For reasons of discreteness, these results are presented separately from the main findings. Snapshots of instantaneous particle velocity provide handy information about clustering of particles, influence of gravity and strength of turbulent dispersive forces. In fig. 5.11, in the start-up phase, gravity pulls particles to the bottom of the tank; and arguably from 5.11c, if the duration of the pre-turbulence phase was any longer most if not all particles will be lying at tank bottom. Also observe the thick multi-layer of particles that develops at tank bottom at $tN = 5$.

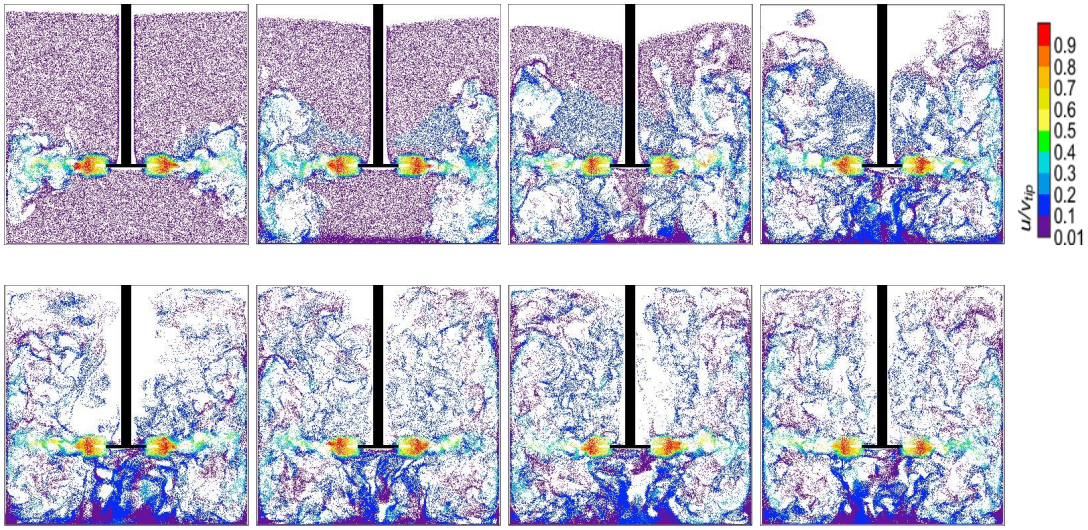

Figure 5.11: Dense suspension simulation of $\Phi_m = 6.63\%$. Particle velocity snapshots in vertical mid-baffle slice of thickness $0.01T$ from top left to right and down: $tN = 2\frac{1}{2}, 5, 7\frac{1}{2}, 10, 12\frac{1}{2}, 20, 25, 30$ for shear-thinning at $n = 0.85$, Re= 8.5×10^3 and Stk=8.24×10^{-2}.

When turbulent conditions finally set in ($tN = 10$ and thereafter), eddies – primarily in the upper circulating loop – can be seen "lifting" particles as high as the top of tank. The strength of these eddies is best appreciated in the light of the vertical solids concentration profile. Compared to case 2A (same Re), it is seen that both Newtonian and shear-thinning examples with high loadings the solids bottom concentration is far lower than cases with lower loading. The reason for this is not entirely clear. Another feature observed in the dense suspensions is the high particle-liquid slip velocities which consequently translates to higher particle Reynolds number. It is tempting to conclude that these observations, in concentration profile and Re_p, is as a result of modification of liquid turbulence by particle flow field and/or particle-collisions. The former, a feature of two-way coupled flows and latter four-way coupled flows where particle contacting is also an issue and hence usually applied to dense suspensions and granular flows. The reader is however reminded that in this work simulations are one-way coupled and there is no feed-back of particle flow field to the liquid. Missed collisions –described in section 5.2, in the suspension with higher loading were also higher (by factor of 2) as in 6.17% and 12.65% in the Newtonian at Re= 8.5×10^3; and also 6.94% and

13.60% in the shear-thinning suspensions. As explained earlier, missed collision procedure is executed when two approaching particles will be closer than d_p in the next time step, so it can be seen that in the simulation of dense suspension particle contacting is important. In this regard four-way [11, 12] coupling should be applied for this system. Contours of particle Reynolds number are shown in fig. 5.12.

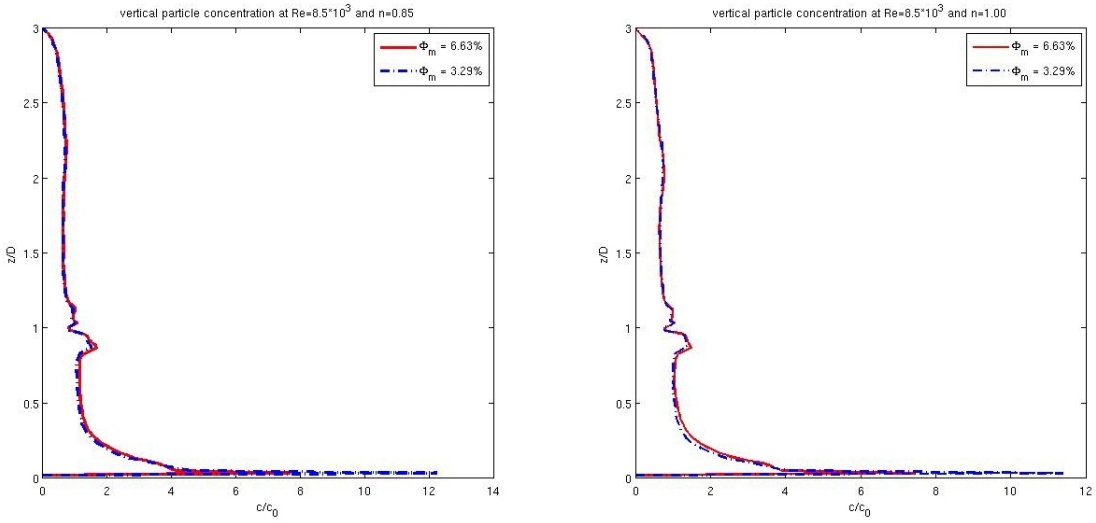

Figure 5.12: Vertical solids concentration: effect of high solids loading. (5.12a) shear-thinning suspension at$n = 0.85$ and Re=8.5×10^3; (5.12b) Newtonian suspensions also at Re=8.5×10^3.

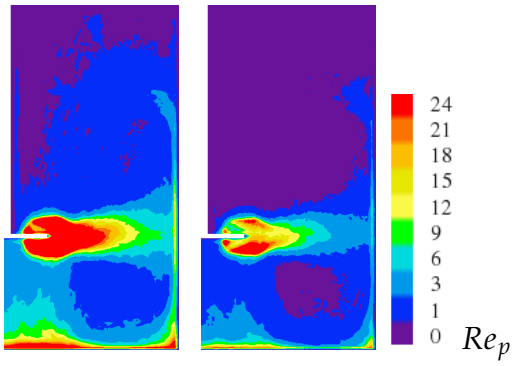

Figure 5.13: Contours of particle Reynolds number Re_p for the dense suspension, $\Phi_m = 6.63\%$, and base case loading shown left. Both simulations were at n=0.85, Stk=8.24×10^{-2} and Re=8.5×10^3. High slip velocities in the dense suspension results in high particle Reynolds number.

5.4 Conclusion and Outlook

The settling and distribution of inertial particles in non-Newtonian liquids agitated with Rushton turbine in a lab-scale tank has been investigated. The non-Newtonian models used in this work are the simplest commonly occurring types in oil sands operations. Since these operations usually are in the turbulent regime, the simulations explore three degrees of Re: $6 \times 10^3, 8.5 \times 10^3$ and 1.25×10^4, i.e. from quasi-turbulent to fully turbulent. Our simulations show that:

- for suspensions with power-law liquids, at the same Re, particle concentration at the tank bottom increases with decreasing flow index. Thus, shear-thinning suspensions recorded highest concentration at the tank bottom, followed by Newtonian suspensions; shear-thinning suspensions recorded least bottom concentration of particles. This observation was seen to be consistent with respect to Reynolds number as all three Re explored produced this behavior.

- increasing the Reynolds number, caused significant increase in bottom concentration of particles. However, given the fact that the same tank and impeller speed is employed, this statement could also be framed as, using less viscous liquids for the same suspension can cause increase in bottom particles.

- suspensions with yield-stress liquids expectedly recorded lower bottom particle concentration. The Herschel-Bulkley model with $n > 1$ behaved as if it had no yield stress by not forming a cavity and holding more particles at tank bottom than those with $n < 1$.

- viscous effects played little to no role in the settling and distribution of solids in the non-Newtonian liquids without yield stress; net gravity rather, played the dominant role in the settling of solids. This is observed in the simulations with reduced solid-liquid density ratio where solids were found to be less concentrated at the bottom than base case simulations.

- when the solids mass fraction was doubled, higher slip-velocities and rather much lower bottom particle concentration are observed. The concentration field is much distributed than at the base case mass fraction. This observation however, needs more insight especially as these simulations are one-way coupled; in two-way coupled simulation the particles will likely attenuate the liquid flow turbulence given the fact that $d_p/D < 0.1$ [11].

In general, faster stirring is known to increase suspension homogeneity [10] in Newtonian systems and cause the opposite effect in suspensions with Bingham liquids [4]. It will be interesting to examine this effect in power-law and Herschel-Bulkley fluids in our simulations. Then also, since the grand objective of this project is to acquire insight into impact of non-Newtonian behavior of oil sands tailing, future work should deal with higher solids mass fraction in the proximity of 10%.

Bibliography

[1] Venneker, B.C.H., Derksen, J.J., Van den Akker, H., "Turbulent non-Newtonian Flow in a Stirred Tank-LDA Experiments on the influence of Reynolds Number and Flow Index", Chemical Engineering Research and Design, Preprint, 2008

[2] Crowe, C.T., "Multiphase Flow Handbook", CRC Press, ISBN 0849312809, 2003

[3] Picciotto, M., Giusti, A., Marchioli, C., Soldati, A., "Turbulence Modulation by Micro-Particles in Boundary Layers ", Proceedings of the IUTAM Symposium on Computational Multiphase, Flow, 53-62, 2006

[4] Derksen, J.J., "Solid Particle Mobility in agitated Bingham liquids", Industrial & Engineering Chemistry Research, 48, p2266, 2009

[5] Metzner, A.B., Otto, R.E., "Agitation of non-Newtonian liquids", AICHE Journal 3, 3, 1957

[6] Zwietering, T. N., "Suspending of Solid Particles in Liquid by Agitators", Chem. Eng. Sci., 8, 244, 1958

[7] Derksen, J. J., H. E. A. Van den Akker, ''Large Eddy Simulations on the Flow Driven by a Rushton Turbine'', AIChE J., 45(2)209., 1999

[8] Schiller, L., Naumann, A., "Uber die grundlagenden Berechnungen bei der Schwerkraftaubereitung", Ver. Deut. Ing. Z., 77, 318, 1933

[9] Derksen, J.J., "Numerical Simulation of Solids Suspensions in a Stirred Tank", AICHE J., vol. 49, 11, 2003

[10] Rieger, F., Ditl, P., Havelková, O., Proceedings of the Sixth European Conference on Mixing Pavia, Italy, pp. 251–258, 1988

[11] Crowe, C., Sommerfeld, M., Tsuji, Y., "Multiphase Flows with Droplets and Particles", CRC Press LLC, 1998

[12] Elgobashi, S., "On Predicting Particle-Laden Turbulent Flows", App. Sci. Res., 52, 309-329, 1994

6 Conclusions and Outlook

6.1 General Discussion

The work presented in this thesis forms part of a broader research to investigate the impact of non-Newtonian behavior on oil sands tailings. Because tailings exhibit a broad spectrum of non-Newtonian characteristics − shear-thinning/thickening, yield stress, time-dependency − the initial phase of the research focused on incorporation of purely viscous (i.e. without time-dependency and memory of shear history) non-Newtonian characteristics into liquid phase. The first systematic work was done with Bingham liquids [1], and my task was to continue with shear-thinning/thickening and Herschel-Bulkley fluids.

In order to put this work into proper academic context, it was decided to begin with single phase agitation of the selected liquids since the literature was barren with non-Newtonian turbulence. The scope at this phase to say the least was bound by what (was there.) Starting with agitation of dynamically similar (same agitation system and at Re=6×10^3) Newtonian, shear-thinning, shear-thickening and Bingham liquid flows in base case simulations, results from this batch of simulations prompted further investigation into the flow index. This enabled direct comparisons of results to data in the literature about shear-thinning velocity profiles. In the second phase of the work, solid particles were introduced into the tank and agitated. The modeling of this two-phase flow followed the Eulerian/Lagrangian approach. The main findings of this work are summarized below.

6.2 Single phase non-Newtonian agitation

- Viscous characteristics of non-Newtonian liquids govern the characteristics of the flow structures observed during the agitation of these liquids. The turbulent flow structures of shear-thickening liquid however, closely resembled that of Newtonian liquid. Cavern formation for shear-thinning liquids observed experimentally at $n < 0.3$ is seen in this work at $n = 0.5$ and Re=6×10^3.

- Although similar structures were seen in the contours of turbulent kinetic energy, k for the shear-thinning/thickening and Newtonian liquids, the differences in these structures were analyzed in terms of percentage of high k regions. It is observed that the Newtonian liquid had the highest percentage in terms of high k regions, followed by the shear-thickening $(n = 1.5)$ and then shear-thinning $(n = 0.5)$.

- Expecting the viscous dissipation trend to reflect these differences in the turbulent kinetic energy (TKE) structures, viscous dissipation was estimated for the three different liquids at Re=1.25×10^4. The trend did not support the observed differences in the kinetic energy contours as it showed the Newtonian liquid having the highest dissipation rate, followed by the shear-thinning and shear-thickening. This was traced to the extra terms in the TKE equation of non-Newtonian liquid which constitute (viscous) diffusion in the turbulent kinetic energy as well as reduced dissipation. See appendix for details.

- Simulations compare well to the empirical correlations for shear-thinning liquids found in the literature. Results from these simulations indicate the radial and tangential mean disk height profiles exhibit a slight dependency on n. The widening effect of profile with n observed experimentally is also seen in our simulation for the radial and tangential profiles. Then, in addition to the tangential, axial rms velocity profile also shows a weak dependency on n.

- The power number for shear-thinning liquids of different n but at the same Re, gives reasonable agreement with measurements in the literature.

6.3 Solid particle motion in turbulently agitated non-Newtonian liquids:

- Particles consistently showed a higher preference for settling at tank bottom in shear-thinning suspensions than in Newtonian and shear-thickening suspensions. At the same Re, particle concentration at the tank bottom increases with decreasing flow index for the power-law liquids. Thus, shear-thinning suspensions recorded highest concentration at the tank bottom and shear-thickening suspensions had the least.

- Increasing the Reynolds number (by using less viscous power-law liquid but at the same n and agitator configuration), caused large increases in bottom concentration of particles. This observation is also valid for the suspension with Newtonian liquid. As anticipated, the suspensions with yield stress (Herschel-Bulkley) fluids had more uniform vertical particle profile and less particle concentration at the tank bottom. Among these fluids, when the flow index $n > 1$, the fluid behaved like it had no yield stress in not forming a cavern (as observed in the velocity snapshots and turbulent kinetic energy). It also held more particles at tank bottom than those with $n < 1$.

- At the same Re, when a denser liquid is used so as to analyze the impact of reduce the solid-liquid density ratio, there is less particles at tank bottom. Although this outcome is not unexpected; it nullifies our initial assumption that non-Newtonian effects (in the viscous sublayer) could be responsible in the high solids concentration at tank bottom in suspensions with non-Newtonian liquids. The new picture formed out of averaged vertical profiles of both solids concentration and viscosity indicates a certain trend. Getting to the tank bottom, the relative viscosity of non-Newtonian liquids decreases

getting further less than unity (shear-thinning lesser than shear-thickening) while solids concentration increases. In effect, the increase in bottom solids concentration is a response of weakened viscous resistance as particles are pulled to the bottom by net gravity force. This explains why using a denser liquid will result in reduced bottom solids concentration in both Newtonian and non-Newtonian liquids since buoyant forces are higher now and diminishes net gravity force.

- The simulations with denser liquid also served a second purpose in studying the effect of particle Stokes number, Stk. At Re=1.25×10^4 both Newtonian and shear-thinning ($n = 0.85$) suspensions with Stk=1.21×10^{-1} recorded more bottom solids concentration than Stk=8.24×10^{-2}.

- When the solids mass fraction was doubled, higher slip-velocities and rather much lower bottom particle concentration is recorded. The concentration field is much more distributed than at the base case mass fraction. This observation however, needs more insight especially as these simulations are one-way coupled.

6.4 Outlook

- For the base case simulations, it was predicted on the basis of their dynamic similarity that flow structures will exhibit to a fair extent high structural similarity (except at the boundaries and at the small scales). Nonetheless, subtle differences were observed in the turbulent kinetic energy, Reynolds stresses and anisotropic contours for these liquids. These differences is believed to stem from the physics at the small scales. The small scales here refers to the Kolmogorov scale where viscosity is important. In the base case simulation for instance, the calculated Kolmogorov size is $\eta_K = L \cdot Re^{-3/4}$ (where L is the characteristic length scale usually taken to be impeller diameter D) which is about 0.114mm, however, the spatial resolution $\Delta = T/180$ of the simulation

corresponds to a linear size of 1.3mm and thus, the dynamics of the scales below this resolution will be "low pass filtered".

- One can counter the argument above by making the case that in DNS, it is possible to capture flow dynamics precisely even if the flow does not resolve the smallest scale. Moin & Mahesh [2] have argued that the η_K restriction on DNS is too stringent and that the resolved small scale should be of the order of η_K i.e. $O(\eta_K)$. In fact in spectral DNS of curved channel flow [3], most dissipation occured at scales greater than $15\eta_K$. This could be true for lattice-Boltzmann simulations too, however until it is confirmed by practice, the small scales cannot be ignored.

- Two-way coupling will, to a large extent be more beneficial for this work in unlocking the local particle-liquid interaction. This should combine with a decent spatial resolution and Kolmogorov scale (η_K of about the size of particle). This will ensure that velocity gradients induced at the particle surface is resolved and not "overwhelmed" [4] by the turbulent liquid flow.

- Then also, it would be interesting looking at how more accurate (higher parameter models e.g. Carreau, Ellis models etc) for the shear-thinning and shear-thickening liquids will perform in contrast to the power-law model.

- Last point concerning liquids, future work should explore complex rheologies likes thixotropy and elasticity, the former is a common characteristic of certain tailings.

- As there are no correlations for drag force on particles in turbulent non-Newtonian liquids, the local particle Reynolds number are derived with local apparent viscosity of the liquid and then used in calculating the drag force. In general, the literature of hydrodynamic forces on single particle mobility in turbulent non-Newtonian fluid is pretty empty. Although not connected, future research should aim at deriving correlations for these forces experimentally or computationally. In addition to applying appropriate correlations

and forces, hydrodynamic force interactions due to multi-particles should be considered in future work as single particle correlations have been used in these simulations.

- In order to elicit a more practical model of tailings, the fines phase should have to be considered. In this work, the fines was assumed to be non-settling and homogeneous with the liquid phase. One can easily predict in any realistic turbulent two-way coupled model of tailings with fines present, the fines will contribute to attenuating the turbulence and in industrial processes this might have consequences for power and energy input into the agitation system. Then again, it should also be emphasized that the non-settling nature of the fines is due to the presence of surface forces that keep the fine particles as distributed as much as possible in the suspension due to long range repulsive forces. In this regard, a good model of tailings fines must take these surface forces into consideration to avoid simulating a bidispersed particle phase. In that case, the resultant flow field will be the same as a simulation with the median size of both particles.

- In reality, the task of simulating tailings flow is not an easy task not only from modeling point of view. The computational resources required for a lab-scale tank, as in this work, is beyond current and near future capabilities. Considering the fact that tailings have high solids loading [5] 55% (of which 82% is course and 17% is fines) and also have residual bitumen present in the liquid phase, a mesoscale simulation approach will be most practical in fully understanding the particle mobility in tailing systems.

Bibliography

[1] Derksen, J.J., “Solid Particle Mobility in agitated Bingham liquids”, Industrial & Engineering Chemistry Research, vol. 48, p2266, 2009

[2] Moin, P., Mahesh, K., “Direct Numerical Simulation: A Tool in Turbulence Research”, Annu. Rev. Fluid Mech., 30, 539-578, 1998

[3] Moser, M.D., Moin, P., “Effect of Curvature in Wall-bounded Turbulent Flows”, J. Fluid Mech. 175:479–510, 1987

[4] Ten Cate, A., Derksen, J.J., Portela, L.M., Van den Akker, H.E.A., “Fully Resolved Simulations of Colliding Monodisperse Spheres in Forced Isotropic Turbulence”, J. Fluid Mech., 519, 233-271, 2004

[5] Beier, N., Sego, D., ”Dewatering of oil sands tailings using Cross Flow Filtration”, GeoEdmonton08, 2008

Appendix

Derivation of turbulent kinetic energy equation for generalized Newtonian fluids as well as Newtonian fluids

Given the incompressible Navier-Stokes:

$$\frac{\partial \tilde{u}}{\partial t} + \tilde{u_j}\frac{\partial \tilde{u_i}}{\partial x_j} = -\frac{1}{\rho}\frac{\partial \tilde{p}}{\partial x_i} + \frac{\partial}{\partial x_j} 2\tilde{\nu_a}\tilde{s_{ij}} \tag{A-1}$$

where $\tilde{s_{ij}} = \frac{1}{2}\left(\frac{\partial \tilde{u_i}}{\partial x_j}\right)$; $\tilde{u} = U + u$; $\tilde{p} = P + p$ where capital symbols denote averaged quantities/variables, lower case representing fluctuating values of the turbulent variables. The instantaneous kinematic viscosity $\tilde{\nu_a}$ can also be expressed as $\tilde{\nu_a} = \nu + \nu_a$ where ν is the average apparent viscosity and ν_a is the fluctuating apparent viscosity [1]. Expanding the instantaneous expression above yields

$$\frac{\partial (U_i + u_i)}{\partial t} + (U_j + u_j)\frac{\partial (U_i + u_i)}{\partial x_j} = -\frac{1}{\rho}\frac{\partial (P + p)}{\partial x_i} + 2\frac{\partial}{\partial x_j}(\nu + \nu_a)\left(S_{ij} + s_{ij}\right) \tag{A-2}$$

time averaging (A-2) yields

$$\frac{\partial U_i}{\partial t} + U_i\frac{\partial U_i}{\partial x_j} + \frac{\partial \overline{u_i u_j}}{\partial x_j} = -\frac{1}{\rho}\frac{\partial P}{\partial x_j} + 2\frac{\partial}{\partial x_j}\left(\nu S_{ij} + \overline{\nu_a} S_{ij} + \overline{\nu_a S_{ij}}\right) \tag{A-3}$$

subtracting (A-3) from (A-2) gives

$$\frac{\partial u_i}{\partial t} + U_j\frac{\partial u_i}{\partial x_j} + u_j\frac{\partial U_i}{\partial x_j} + u_j\frac{\partial u_i}{\partial x_j} - \frac{\partial \overline{u_i u_j}}{\partial x_j} = -\frac{1}{\rho}\frac{\partial p}{\partial x_j} + 2\frac{\partial}{\partial x_j}\left[\nu s_{ij} + \nu_a S_{ij} + \nu_a s_{ij} - \overline{\nu_a} S_{ij} - \overline{\nu_a s_{ij}}\right] \tag{A-4}$$

multiplying through by u_i followed by substitution of $k = \frac{1}{2}\overline{u_i u_i}$ and then averaging yields

$$\frac{\partial k}{\partial t} + U_j\frac{\partial k}{\partial x_j} + \overline{u_i u_j}\frac{\partial U_i}{\partial x_j} - u_j\frac{\partial k}{\partial x_j} = -\frac{1}{\rho}\frac{\partial \overline{p u_i}}{\partial x_j} + 2\left[\overline{u_i\frac{\partial}{\partial x_j}\nu s_{ij}} + \overline{u_i\frac{\partial}{\partial x_j}\nu_a S_{ij}} + \overline{u_i\frac{\partial}{\partial x_j}\nu_a s_{ij}}\right] \tag{A-5}$$

the terms in the brackets can be processed further in the manner similar to this example, e.g. $\overline{u_i\frac{\partial}{\partial x_j}\nu s_{ij}} = \frac{\partial}{\partial x_j}\overline{u_i \nu s_{ij}} - \overline{\nu s_{ij} s_{ij}}$ implementing this rule in (A-5) gives

$$\underset{I}{\frac{\partial k}{\partial t} + U_j\frac{\partial k}{\partial x_j}} = \underset{II}{-\frac{1}{\rho}\frac{\partial \overline{p u_i}}{\partial x_i}} \quad \underset{III}{-\overline{u_i u_j}\frac{\partial U_i}{\partial x_j}} \quad + \quad \underset{IV}{\frac{\partial}{\partial x_j}\left(-\frac{1}{2}\overline{u_j u_i^2} + 2\nu\overline{u_i s_{ij}} + 2\overline{\nu_a u_i} S_{ij} + 2\overline{\nu_a u_i s_{ij}}\right)}$$
$$\underset{V}{-\left(2\nu\overline{s_{ij}s_{ij}} + 2\overline{\nu_a s_{ij}} S_{ij} + 2\overline{\nu_a s_{ij} s_{ij}}\right)}$$

The usual interpretations for the various terms are:

I – rate of change of kinetic energy (with time and convection)

II – transport of TKE by pressure fluctuations

III – shear production of TKE, note that sign is reversed so that $-\overline{u_i u_j}\frac{\partial U_i}{\partial x_j}$ to represent a gain to TKE

IV – diffusion of TKE due to turbulence itself $\left(-\frac{1}{2}\overline{u_j u_i^2}\right)$ and viscous stresses

V – viscous dissipation of TKE

In the case of Newtonian liquid, (A-1) is written as:

$$\frac{\partial \tilde{u}}{\partial t} + \tilde{u_j}\frac{\partial \tilde{u_i}}{\partial x_j} = -\frac{1}{\rho}\frac{\partial \tilde{p}}{\partial x_i} + \frac{\partial}{\partial x_j} 2\nu\tilde{s_{ij}} \tag{A-6}$$

When the steps above are repeated for (A-6) keeping in mind the viscosity is constant, the final equation for the turbulent kinetic equation for a Newtonian liquid becomes

$$\frac{\partial k}{\partial t} + U_j \frac{\partial k}{\partial x_j} = -\frac{1}{\rho}\frac{\partial \overline{pu_i}}{\partial x_j} - \overline{u_i u_j}\frac{\partial U_i}{\partial x_j} + \frac{\partial}{\partial x_j}\left[-\frac{1}{2}\overline{u_j u_i^2} + 2\nu\overline{u_i s_{ij}}\right] - 2\nu\overline{s_{ij}s_{ij}} \qquad \text{(A-7)}$$

Shear-thinning flow index effect on the fluid rheology: simple parameter study

Assuming the power-law model for the shear-thinning fluid, the shear stress given by: $\boldsymbol{\tau} \equiv -\boldsymbol{\eta}\dot{\gamma}$ now becomes $\boldsymbol{\tau} = K\dot{\gamma}^n$. The plot of τ vs $\dot{\gamma}$ below shows that keeping K constant, the viscous behavior at low n is very similar to that of yield-stress fluids.

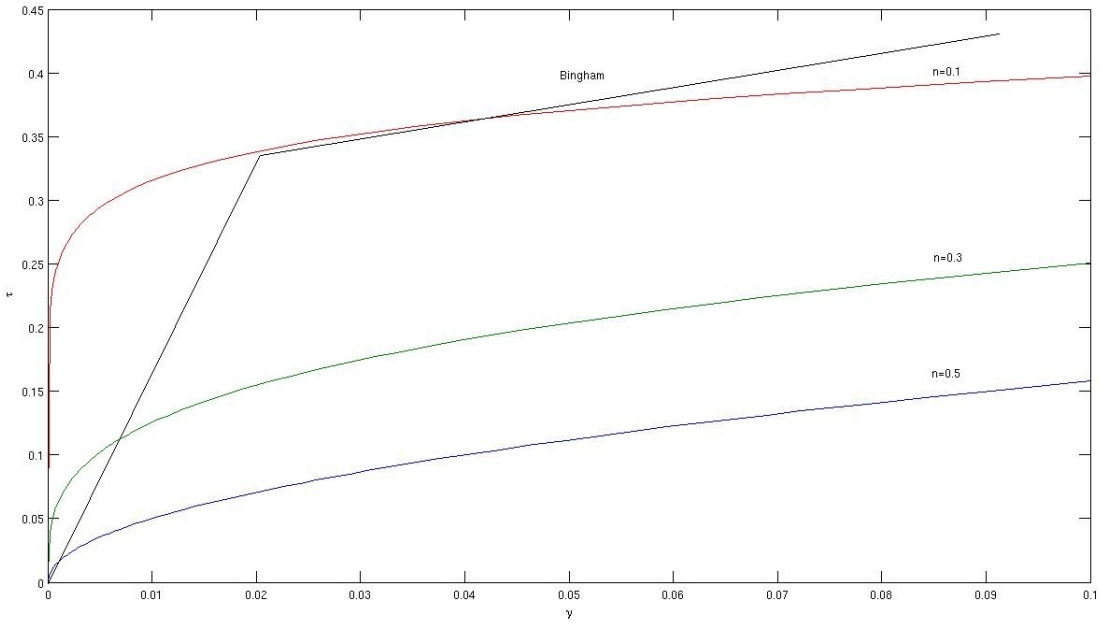

Figure A-1: Viscous behavior of shear-thinning liquids with at same K but with varying n, the Bingham line shows proximity of the $n = 0.1$ case to the bi-viscosity model used in implementing the Bingham liquids in this thesis.

Bibliography

[1] Pinho, F.T., Whitelaw, J.H., “Flow of non-Newtonian Fluids over a Confined Baffle”, J. Fluid Mech., 226, p475-496,1991